Preprint notice

This manuscript is a non-peer-reviewed preprint submitted to EarthArXiv.

Title: Linking double seismic zones to oceanic lithosphere rheological layering: the role of mid-lithospheric discontinuities

Authors: Tianyu Hu[1], Zhensheng Wang[1]*, Junfeng Zhang[1]*, Feng Shi[1], Fabio Capitanio[1,2], Xinnuo Li[1], Sierd Cloetingh[3,4], István J. Kovács[3], Alessio Lavecchia[3,5,4], Alexander Koptev[6,3]

Affiliations:

[1]State Key Laboratory of Geological Processes and Mineral Resources, Center for Global Tectonics, School of Earth Sciences, China University of Geosciences, Wuhan, China.

[2]School of Earth, Atmosphere and Environment, Monash University, Clayton, Victoria, Australia.

[3]Institute of Earth Physics and Space Science ELKH, Sopron, Hungary.

[4]Department of Earth Sciences, Utrecht University, Utrecht, The Netherlands.

[5]University of Bari "Aldo Moro", Bari, Italy.

[6]State Key Laboratory of Critical Earth Material Cycling and Mineral Deposits, School of Earth Sciences and Engineering, Nanjing University, Nanjing, China.

***Corresponding author:** Zhensheng Wang (Email: jasonwang@cug.edu.cn); Junfeng Zhang (Email: jfzhang@cug.edu.cn)

Abstract

The origin of the ubiquitous lower seismic layer (LSL) in double seismic zones (DSZs) within subducting oceanic lithosphere remains one of the most persistent unresolved problems in subduction-zone seismicity. Analysis of recent geophysical observations reveals a close spatial association between the LSL and the oceanic mid-lithospheric discontinuity (MLD), a feature attributed to the accumulation and crystallization of residual or intrusive melts within oceanic lithosphere, suggesting a genetic link between the two structures. Here, combining observational constraints with geodynamic numerical modeling, we show that melt crystallization and subsequent metamorphic reactions within the MLD promote grain-size reduction and rheological layering, which localize differential stress in the mantle section above the MLD. These processes create favorable conditions for earthquake generation and naturally explain the development and features of the LSL. Importantly, this mechanism does not require a hydrated lower seismic layer, consistent with seismic observations from numerous subduction zones worldwide.

Keywords: Double seismic zone; Lower seismic layer; Oceanic mid-lithospheric discontinuity; Eclogitization; Differential-stress amplification; Apparent friction coefficient

1. **Introduction**

Global seismic observations show that intermediate-depth earthquakes define the Wadati–Benioff zone within subducting slabs (Benioff, 1949). In many subduction zones, this seismicity is further resolved into two subparallel dipping planes at depths of ~70–300 km, forming double seismic zones (DSZs) (Fig. 1A) (Brudzinski et al., 2007; Peacock, 2001; Zhan, 2020). The formation of the upper seismic layer (USL) is generally attributed to dehydration embrittlement associated with hydrous mineral breakdown (Hacker et al., 2003; Kirby et al., 1996), whereas the origin of the lower seismic layer (LSL) remains debated (Peacock, 2001; Shi et al., 2022; Zhan, 2020). Proposed mechanisms include dehydration embrittlement associated with antigorite breakdown (Jung et al., 2004; Mishra and Zhao, 2004; Peacock, 2001; Yamasaki and Seno, 2003), thermal stresses related to slab bending and unbending (Goto et al., 1985; Hamaguchi et al., 1983), shear instabilities in dry olivine (John et al., 2009; Kelemen and Hirth, 2007), metastable phase transformations involving Al-rich orthopyroxene (Dera et al., 2013; Kirby et al., 1996), and metamorphic embrittlement related to orthopyroxene (Opx) reactions (Shi et al., 2022). However, the strong regional variability of LSL geometry, depth, and hydration signatures suggests that no single mechanism fully explains its global characteristics (Brudzinski et al., 2007; Florez and Prieto, 2019; Peacock, 2001; Sippl et al., 2022; Zhan, 2020).

One emerging perspective is that the LSL may be fundamentally governed by

rheological layering within subducting lithosphere (Shi et al., 2022; Toffol et al., 2022). Oceanic plates inherently develop layered structures before subduction through both thermal evolution and compositional differentiation (Chen et al., 2024; Tharimena et al., 2017; Turcotte and Schubert, 2002). Thermal aging produces systematic variations in temperature and viscosity, resulting in age-dependent rheological layering of the lithosphere (Ranalli, 1995; Turcotte and Schubert, 2002). In addition, melt extraction and infiltration processes generate compositional heterogeneities within the oceanic lithosphere, producing mechanically distinct layers that may further modify deformation and stress distribution during subduction (Chen et al., 2024; Liu et al., 2026; Ohira et al., 2017; Tharimena et al., 2017).

Recent seismic studies have revealed widespread seismic low-velocity zones at mid-lithospheric depths (~30–80 km) beneath oceanic basins, referred to as oceanic mid-lithospheric discontinuities (MLDs) (Fig. 1A, B) (Chen et al., 2024; Liu et al., 2026; Ohira et al., 2017; Tharimena et al., 2017). These discontinuities are commonly interpreted as resulting from the crystallization and metamorphism of small amounts of mantle melts embedded in a peridotite matrix, including both residual and intruded melts, thereby forming potential compositional and rheological interfaces (Chen et al., 2024; Kovács et al., 2021; Liu et al., 2026; Ohira et al., 2017; Tharimena et al., 2017). During subduction, this interface may be carried into the mantle together with the downgoing slab, where it is positioned immediately below the LSL according to their depth from the slab top (Fig. 1B, C). This striking spatial correspondence likely

suggests that pre-existing rheological layering inherited from oceanic lithosphere may influence the development of intermediate-depth seismicity. However, whether and how the MLD controls stress localization and earthquake generation within slabs remains unexplored.

Here, we use two-dimensional thermo-mechanical numerical models to investigate how lithospheric rheological layering influences intermediate-depth seismicity, with particular focus on the role of oceanic MLDs. By comparing models with different thermal structures and slab ages, as well as models with and without melt-derived compositional layering, we demonstrate that a subducted MLD can reorganize stress distribution within slabs and generate a mechanically favorable condition for LSL formation. Our results show that melt-derived MLDs and their subsequent eclogitization during subduction generate rheological layering that provides an alternative explanation for key characteristics of the LSL, including its depth, geometry, spatial distribution, stress state, and variations in hydration signatures.

2. Methods

2.1. Conservation equations and model conditions

We employ 2-D geodynamic models to simulate the subduction of an oceanic slab and its embedded MLD. The numerical models are built using the finite-element particle-in-cell framework Underworld 2 (Moresi et al., 2003) to solve the conservation equations of mass (1), momentum (2), and energy (3):

$$\nabla \cdot u = 0 \quad (1)$$

$$\nabla \cdot [\eta(\nabla u + \nabla u^T)] - \nabla P = -\rho g \quad (2)$$

$$\rho C_p(\frac{\partial T}{\partial t} + u\nabla T) - \nabla(k\nabla T) = -\alpha\rho v_z T \quad (3)$$

where u is velocity, P the pressure, T the temperature, η the viscosity, ρ the density, g the gravitational acceleration, C_p the specific heat capacity, t the time, κ the thermal conductivity, α the coefficient of thermal expansion, v_z the vertical component of velocity. The thermal conductivity (κ) is defined as a function of temperature (T) and pressure (P) (Tosi et al., 2013). Detailed parameter values are provided in Tables S1 and S2.

$$k = (d_0 + d_1 P)(\frac{300}{T})^{d_2} \quad (4)$$

The numerical models span 660 km in depth and 4000 km in length, with a spatial resolution of 2 × 2 km and ~30 Lagrangian particles per finite-element cell. The model domain consists of a convecting mantle overlain by an oceanic plate extending ~3000 km in length (Fig. 2A-D). To initiate subduction, the leading edge of the slab is prescribed with an initial bending geometry. The initial temperature field is prescribed using a half-space cooling model (Turcotte and Schubert, 2002), with cooling age linearly increasing from 0 Ma at the right boundary to the assigned slab age (t_{slab}) toward the trench (Fig. 2A). The top boundary is free-slip with a fixed temperature of 273 K on the plate top surface. The temperature field of the ambient mantle and related boundaries follows the adiabatic geotherm (Fig. 2A, E) (Katsura et al., 2010). The bottom boundary is fixed, and the lateral walls are periodic.

2.2. Material field and model groups

The slab consists of a 7 km thick oceanic crust, and a 93 km thick lithospheric mantle. In models containing an MLD, the prescribed MLD layer (35 km thick) subdivides the lithospheric mantle into upper (28 km thick) and lower portions (30 km thick).

Oceanic MLDs are interpreted to consist predominantly of peridotite containing small amounts of crystallized and metamorphosed mantle melts, commonly represented by garnet granulites (Chen et al., 2024; Ohira et al., 2017; Tharimena et al., 2017) or pargasites (Kovács et al., 2021). These melt-derived components are thought to originate either from residual melts trapped along grain boundaries during mid-ocean ridge spreading (Chen et al., 2024; Ohira et al., 2017; Rychert et al., 2021), or from melts subsequently intruded from the asthenosphere during later stages of plate evolution (Tharimena et al., 2017). For simplicity, we hereafter refer to these lithologies collectively as garnet granulites. Based on these observations and interpretations, we constructed three groups of numerical models to investigate the mechanical effects of melt-derived MLDs during subduction (Figs. 2B-D).

Group 1 (Fig. 2B) represents a reference group without an MLD, corresponding to a classical oceanic lithospheric structure during subduction. In this configuration, slab rheology is governed only by temperature- and pressure-dependent processes, allowing us to isolate intrinsic thermal-rheological layering without additional compositional heterogeneity introduced by an MLD. Because the thermal structure of

oceanic lithosphere evolves with plate ages, we consider a range of slab ages in this group to investigate the effects of age-dependent thermal-rheological layering.

Group 2 (Fig. 2C) represents models in which the MLD consists of a peridotitic matrix containing small amounts of intergranular granulites derived from crystallization of residual melts (Chen et al., 2024). Similar to Group 1, models with different slab ages are considered to account for the influence of age-dependent thermal structures and to enable direct comparison between MLD-bearing and MLD-free cases. The abundance of these residual-melt–derived granulites is prescribed to vary from 0–4% across the MLD layer (Chen et al., 2024; Sizova et al., 2010), following the mantle melting models (Katz et al., 2003), and consistent with geophysical observations of oceanic MLDs (Ohira et al., 2017; Tharimena et al., 2017).

Group 3 (Fig. 2D) builds on Group 2 (Chen et al., 2024) by additionally incorporating granulites derived from intrusive mantle melts (Tharimena et al., 2017). As in Groups 1 and 2, a range of slab ages is considered to isolate the effects of compositional heterogeneity from variations in thermal structure. Consistent with geophysical observations of oceanic MLDs (Ohira et al., 2017; Tharimena et al., 2017), these intrusive granulites are represented by randomly distributed keel-shaped ellipsoidal bodies composed entirely of granulite, with major and minor axes of 8 km and 4 km, respectively. The bodies are emplaced within the lithospheric mantle near the hydrous basalt solidus (Schmidt and Poli, 1998). All models incorporate experimentally constrained lithological properties and phase-transition parameters associated with

compositional heterogeneity within the slab.

2.3. Density

The density of rocks is expressed as a function of temperature (T) and pressure (P), including density variations associated with eclogitic phase transitions (Xiang et al., 2021):

$$\rho = \rho_{depth}\,(1 - \alpha \Delta T) \tag{5}$$

$$\alpha = (a_0 + a_1\,T + a_2\,T^{-2})exp(-a_3\,P) \tag{6}$$

ρ_{depth} denotes the reference density of peridotite ($\rho_{\text{depth\_per}}$) or oceanic crust / granulite / eclogite ($\rho_{\text{depth\_mafic}}$) along mantle adiabat (Fig. 2F) (Xiang et al., 2021), α the thermal expansion coefficient as a function of temperature (T) and pressure (P), ΔT is the temperature difference relative to the mantle adiabat. a0, a1, a2 are fitting parameters (Tosi et al., 2013).

The density of the MLD originating from residual and intrusive melts is determined using different computational approaches:

$$\rho_{residual} = c \cdot \rho_{mafic} + (1 - c)\rho_{per} \tag{7}$$

$$\rho_{intrusive} = \rho_{mafic} \tag{8}$$

c represents the volume fraction of granulite/eclogite formed by residual melt crystallization and eclogitization (0%-4%), ρ_{per} and ρ_{mafic} denote the density of mantle peridotite and granulite or eclogite calculated via Equation 5, respectively.

2.4. Rheology

We applied a non-linear visco-plastic rheology, where the effective viscosity is defined as the minimum between viscous ($\eta_{viscous}$) and plastic viscosities (η_{yield}), truncated by the prescribed lower (η_{min_model}) and upper (η_{max_model}) bounds of viscosity in the model (Fig. 2G) (Ranalli, 1995)

$$\eta_{yield} = \frac{C_0 + C_1 P}{2\dot{\varepsilon}_{II}} \tag{9}$$

$$\eta_{viscous} = \left(\frac{1}{\eta_{diff}} + \frac{1}{\eta_{disl}} + \frac{1}{\eta_{max\_model}}\right)^{-1} \tag{10}$$

$$\eta_{eff} = min\left(\eta_{viscous}, \eta_{yield}\right) \text{ and:}$$

$$\eta_{eff} = \eta_{min\_model} \quad \text{if} \quad \eta_{eff} < \eta_{min\_model} \tag{11}$$

$$\eta_{eff} = \eta_{max\_model} \quad \text{if} \quad \eta_{eff} > \eta_{max\_model}$$

where $\dot{\varepsilon}_{II}$ the second invariant of the strain rate tensor, C_0 the cohesion, C_1 the internal friction coefficient.

Diffusion creep viscosity (η_{diff}) is defined as a function of pressure (P) and temperature (T), while dislocation creep viscosity (η_{disl}) additionally depends on the second invariant of the strain rate tensor ($\dot{\varepsilon}_{II}$) (Hirth and Kohlstedt, 2003).

$$\eta_{diff} = \frac{1}{A_{diff}} \exp\left(\frac{E_{diff} + PV_{diff}}{RT}\right) \tag{12}$$

$$\eta_{disl} = A_{disl}^{\frac{-1}{n}} \dot{\varepsilon}_{II}^{\frac{1-n}{n}} \exp\left(\frac{E_{disl} + PV_{disl}}{nRT}\right) \tag{13}$$

where A is the pre-exponential factor, n the strain exponent, E the activation energy, V the activation volume, R the gas constant. Detailed parameter values are provided in Table S3.

During subduction, granulites within the MLD undergo eclogitization (fig. S1), a process characterized by grain-size reduction and the activation of diffusion creep and grain-boundary sliding, which triggers a profound rheological weakening and causes the effective viscosity of the newly formed eclogite to drop by several orders of magnitude (McNamara et al., 2024; Stünitz et al., 2020). As metamorphism proceeds, eclogite grains grow, therefore the efficiency of diffusion creep decreases, leading to a progressive increase in viscosity and dislocation creep as favored deformation mechanism (Shi et al., 2018; Stünitz et al., 2020). To model this weakening–recovery process in the geodynamic models, we prescribe a time-dependent diffusion-creep viscosity for eclogitized granulites within the MLD (η_{ecl_diff}). This parameterization is based on the grain-size sensitivity of Coble creep, in which the effective diffusion-creep viscosity scales with the cube of the grain size (Coble, 1963; Hirth and Kohlstedt, 2003). The grain-size evolution of eclogite is unclear, we thus introduce a simplified dimensionless recovery factor (f_t), as a proxy for the grain-growth state after the eclogitization of the MLD:

$$f_t = \min\left(\frac{t_{growth}}{t_{trans}}, 1\right) \quad (14)$$

Where t_{growth} is the cumulative duration of grain growth following eclogitization, t_{trans} is the characteristic timescale over which diffusion-creep viscosity evolves toward its maximum value. As t_{growth} increases, f_t progressively approaches 1, reflecting continued grain growth and the corresponding increase in diffusion-creep viscosity toward its maximum value.

Following the grain-size cubic dependence of diffusion creep (Coble, 1963; Hirth and Kohlstedt, 2003), we scale the viscosity recovery by f_t^3. The diffusion-creep viscosity of eclogitized granulite is then calculated as the minimum viscosity immediately after eclogitization plus a time-dependent viscosity increase associated with grain growth:

$$\eta_{ecl\_diff} = (\eta_{max} - \eta_{min}) f_t^3 + \eta_{min} \quad (15)$$

η_{max} is the maximum viscosity of diffusion creep, and commonly the maximum viscosity for the model (η_{max_model} =10^{25} Pa·s). We systematically explored a broad range of minimum viscosities following eclogitization (η_{min}, 10^{18}–10^{22} Pa·s) and characteristic timescales (t_{trans}, 5–30 Myr) following the phase transformation (Hirth and Kohlstedt, 2003; Kylander-Clark et al., 2007; Shinevar et al., 2015; Skora et al., 2009), thereby encompassing the full spectrum of plausible post-eclogitization grain-growth scenarios. This process exerts an effect on diffusion creep similar to that produced by simultaneous grain growth and grain-size reduction during grain-damage processes (Fig. 2H, I) (Gerya et al., 2021; Liu et al., 2026).

We calculate the viscosity of the finite-element cells with hybrid particles (e.g., the MLD with residual granulites) using a harmonic mean (Huet et al., 2014):

$$\eta_{hybrid} = \left(\frac{c}{\eta_{mafic}} + \frac{1-c}{\eta_{per}} \right)^{-1} \quad (16)$$

η_{per} denote the viscosity of mantle peridotite and η_{mafic} is that of gabbro, granulite or eclogite (based on Equations 9-15 and Table S3).

2.5. Model runs

A total of 79 numerical experiments were conducted. The model suite includes both MLD-absent group (Group 1) and MLD-bearing groups (Group 2 and 3) spanning slab ages of 40–70 Myr. For the MLD-bearing groups, we systematically varied η_{min} (10^{18}–10^{22} Pa s), and t_{trans} (5–30 Myr) (Table S4). This parameter space spans the range of experimentally constrained viscosities and metamorphic timescales relevant to prograde eclogitization (Hirth and Kohlstedt, 2003; Kylander-Clark et al., 2007; Shinevar et al., 2015; Skora et al., 2009).

3. Results

The results of the 79 numerical experiments are organized according to the key parameters explored in this study. We first compare models without an MLD (Group 1), with residual-melt–derived MLD (Group 2) and with additional intrusive-melt–derived MLD (Group 3). We then assess the effects of slab age, followed by systematic tests of the characteristic timescale (t_{trans}) and minimum viscosity following eclogitization (η_{min}).

Across all model groups, a common result emerges: models containing an oceanic MLD consistently develop an intra-slab low-viscosity zone associated with eclogitization of the MLD. This weakened zone localizes deformation within the MLD and promotes differential-stress concentration in the mantle section immediately above it, producing a high apparent-friction-coefficient (high-μ_{app}) band favorable for seismic

247 failure. In contrast, such stress amplification is absent or markedly weaker in models
248 without an MLD, where differential stresses rarely reach the failure threshold expected
249 for dry mantle rocks (Fig. 3). Detailed results are presented below.

250 **3.1. Models without an MLD**

251 The models in Group 1 represent classical oceanic lithospheres without an MLD,
252 with layered thermal and rheological structures determined by the half-space cooling
253 model and slab ages (t_{slab}) described in the methods. Fig. 3A-D presents the results of
254 the reference model with t_{slab}=70 Myr. During subduction, the slab maintains a
255 coherent high-viscosity structure, with most regions exceeding 10^{22} Pa s (Fig. 3A).
256 Correspondingly, deformation within the slab remains limited, with strain rates
257 generally below 10^{-16} s^{-1} (Fig. 3B). The slab-parallel normal stress (σ_{ss}, where *ss*
258 denotes the slab-parallel direction at the mid-slab plane) defines a laterally continuous
259 tensional band at intermediate depths, and the calculated tensional axes (T axes) are
260 generally aligned with the local slab-parallel direction (Fig. 3C). This tensional band
261 extends up to ~50 km beneath the slab top. Peak tensional stresses reach ~800 MPa,
262 whereas most high-stress regions remain below ~300 MPa. The apparent friction
263 coefficient (μ_{app}), calculated from the Mohr-Coulomb stress state (Capitanio et al.,
264 2025; Hackston and Rutter, 2016), reveals two separated bands of relatively elevated
265 values (Fig. 3D). Parts of the upper band locally exceed 0.4, whereas the lower band
266 remains below 0.4 throughout the model.

3.2. Residual-melt MLD models

For the corresponding model in Group 2, the slab configuration is identical to that of the reference model, except for the inclusion of a residual-melt-derived MLD. During subduction, eclogitization of granulites within the residual MLD induces significant weakening and generates a distinct low-viscosity layer within the slab, with most regions of the eclogitized MLD exhibiting viscosities below 10^{20} Pa s (Fig. 3E). The strain-rate field shows that deformation becomes strongly localized within the newly eclogitized MLD, forming a narrow high-$\dot{\varepsilon}_{II}$ band (Fig. 3F) that is absent in the reference model (Fig. 3B). This intra-slab deformation localization is accompanied by a marked change in the stress field. The slab-parallel normal stress (σ_{ss}) defines a spatially continuous tensional lower band extending from ~70 to 200 km depth, but this band is shifted to closer distances from the slab top and concentrated immediately above the MLD (Fig. 3G). The amplified tensional band is mainly located ~20–35 km beneath the slab top, much shallower than those in the MLD-absent model. Peak tensional stresses reach ~4.5 GPa, and extensive regions exceed 500 MPa, substantially higher than those in the MLD-absent model. The calculated T axes remain generally aligned with the local slab-parallel direction. The apparent friction coefficient (μ_{app}) also increases markedly, producing two distinct dipping bands of elevated values (Fig. 3H). In particular, the lower high-μ_{app} band forms immediately above the MLD, with values commonly exceeding 0.4 and local maxima reaching ~0.75. As the slab descends to greater depths, grain growth within the eclogitized MLD progressively reduces its

weakening effect, thereby suppressing strain localization and stress amplification.

3.3. Residual-melt and intrusive-melt MLD models

The corresponding model in Group 3 contains an additional intrusive-melt-derived MLD compared with the one in Group 2. It shows a mechanical pattern (Fig. 3I–L) similar to that of the residual-melt MLD model (Fig. 3E–H). A low-viscosity layer develops within the eclogitized MLD, with locally lower viscosities in the intrusive-melt-derived eclogite domains (Fig. 3I). Deformation is also localized within the MLD, forming a narrow high-$\dot{\varepsilon}_{II}$ band (Fig. 3J). The slab-parallel normal stress (σ_{ss}) is also strongly amplified above the MLD at depths of ~70–200 km, and the calculated T axes remain generally aligned with the local slab-parallel direction (Fig. 3K). The apparent friction coefficient (μ_{app}) is similarly amplified in the slab mantle immediately above the MLD, with most of the lower band exceeding 0.4 and local values reaching ~0.7 (Fig. 3L). Thus, adding intrusive-melt-derived components does not change the first-order mechanical pattern, but further enhances local viscosity reduction within the MLD.

3.4. The influence of slab age

In addition to the 70 Myr models shown in Fig. 3, we further tested models with different slab ages ranging from 40 to 65 Myr (Fig. 4 and fig. S2). The differences between MLD-absent and MLD-bearing models remain systematic. The MLD-absent models with age-dependent rheological layering exhibit similar characteristics across

different slab ages, with zones of elevated tensional stress systematically developing deeper within the slab, typically ~40–50 km below the slab top. However, the magnitudes of σ_{ss} remain relatively low (fig. S2). In contrast, the MLD-bearing models with additional compositional layering consistently develop a shallower, spatially continuous tensional band immediately above the MLD, with substantially amplified σ_{ss} values compared with the MLD-absent models (Fig. 4 and fig. S2). These results indicate that the effect of the MLD on stress localization is robust across a wide range of slab ages.

The apparent friction coefficient (μ_{app}) shows a consistent contrast between the three model groups across different slab ages. MLD-absent models (Group 1) generally exhibit much lower μ_{app}, particularly within the lower band. Only some younger slabs (slab age ≤ 50 Myr) develop a lower-band region with $\mu_{app} > 0.4$ in the MLD-absent models (Fig. 4A–C). Even in these cases, the corresponding μ_{app} values remain substantially lower than those in the MLD-bearing models. In contrast, MLD-bearing (Group 2 and 3) models consistently exhibit two well-separated bands of elevated μ_{app}, with values commonly exceeding 0.4 and extensive regions reaching or exceeding ~0.7 (Fig. 4). Overall, the slab-age tests demonstrate that MLD-bearing models maintain a shallower, stronger tensional band and systematically higher μ_{app} values across the explored age range.

3.5. The influence of t_{trans} and η_{min}

Additional parameter tests show that the slab-parallel tensional band above the MLD and the associated high-μ_{app} double-band structure are robust across the explored parameter space defined by the minimum viscosity following eclogitization (η_{min}) and the characteristic timescale (t_{trans}) (Fig. 5, figs. S3–S5). As η_{min} decreases, indicating stronger weakening, and as t_{trans} increases, indicating a longer persistence of diffusion creep before recovery to dislocation creep, the tensional band above the MLD shifts to shallower depths (figs. S3–S4). Meanwhile, the two high-μ_{app} bands become more clearly separated, and the high-μ_{app} lower band above the MLD becomes more prominent (Fig. 5, fig. S5). Nevertheless, all MLD-bearing models within the explored ranges of η_{min} and t_{trans} consistently develop a tensional band above the MLD and two separated high-μ_{app} bands within the slab. As η_{min} increases to 10^{22} Pas, an additional band of slightly elevated μ_{app} develops at greater depths within the slab.

4. Discussion

4.1. Stress localization and apparent friction enhancement above the MLD

Previous studies have shown that slab bending and unbending associated with age-dependent rheological layering can generate a characteristic double-banded stress structure within subducting slabs, typically consisting of an upper compressional band

347 and a lower tensional band (Fujita and Kanamori, 1981; Goto et al., 1985; Hamaguchi
348 et al., 1983). In some subduction systems, however, both bands may exhibit extensional
349 stress regimes (Sippl et al., 2022). Our MLD-absent models with age-dependent
350 rheological layering produce a similar double-banded stress pattern, with the lower
351 band also characterized by slab-parallel tension. However, this lower tensional band is
352 located deeper within the slab and is associated with substantially lower differential
353 stresses than those in MLD-bearing models. As a result, the predicted stress levels may
354 be insufficient to induce seismic failure in dry mantle peridotite. These results suggest
355 that bending–unbending stresses caused by age-dependent rheological layering alone
356 may not fully explain the occurrence of the LSL, particularly in regions where
357 seismicity develops within dry slab mantle. Some studies also suggest that stresses
358 generated by normal subduction alone are commonly insufficient to trigger
359 intermediate-depth earthquakes, implying that an additional weakening mechanism is
360 often required (Toffol et al., 2022). In our models, eclogitization of the granulites in the
361 MLD provides such a weakening process (Fig. 3E, I). Rather than simply weakening
362 the MLD itself, this rheological contrast localizes deformation within the MLD and
363 shifts stress to the stronger mantle immediately above it. This produces differential-
364 stress amplification in the overlying slab mantle (Fig. 3G, K).

365 This effect is also reflected in the distribution of the apparent friction coefficient
366 (μ_{app}) with depth from the slab top (Fig. 6). In the MLD-bearing models, the high-μ_{app}
367 population is concentrated at ~20–35 km below the slab top, immediately above the

MLD depth range. Many particles exhibit μ_{app} values exceeding 0.4, with some even reaching ~0.75, overlapping the peak friction range (0.4–0.7) required for seismic nucleation during the initial strengthening stage of dry peridotite (Del Gaudio et al., 2009). In contrast, the MLD-absent model shows much lower μ_{app} in the corresponding lower-band region with most particles remaining below 0.4 and distributed deeper in the slab, reaching ~50 km below the slab top. Such conditions generally require a hydrated mantle (μ_{app} <0.4 or less) to facilitate earthquake nucleation. These results show that the MLD focuses differential stress into the overlying slab mantle, shifts the high-μ_{app} lower band to shallower depths, and raises μ_{app} under dry mantle conditions. This provides a dry mechanical pathway toward lower-band brittle failure.

4.2. Comparison between model predictions and observations

Although our models are not designed to reproduce seismicity directly, they provide a mechanical link between the long-term rheological evolution of subducting slabs and the spatial patterns of the LSL. In the MLD-bearing models, the high-μ_{app} lower band develops at depths of ~70–200 km and is located ~20–35 km below the slab top, immediately above the MLD (Figs. 3, 6). This depth range is consistent with the typical geometry and position of the LSL inferred from global and regional double-seismic-zone observations (Brudzinski et al., 2007; Florez and Prieto, 2019; Zhan, 2020). More importantly, our data compilation shows that observed LSLs are systematically positioned above oceanic MLDs of comparable slab ages (Fig. 7A)

389 (Brudzinski et al., 2007; Florez and Prieto, 2019; Tharimena et al., 2017). This observed
390 spatial ordering is modeled by the MLD-bearing models, in which the high-μ_{app} lower
391 band also forms immediately above the MLD.

392 A second point of consistency concerns the depth-dependent decrease in lower-
393 plane seismicity. Observations show that LSL seismicity generally decreases with depth
394 (Fig. 7B) (Zhan, 2020). In our models, particles with $\mu_{app} > 0.4$ also become
395 progressively less abundant at greater depths (Fig. 7C). This trend is in agreement with
396 the progressive recovery of the eclogitized MLD: as grain growth reduces the efficiency
397 of diffusion creep and deformation shifts back toward dislocation creep, weakening
398 diminishes and differential-stress amplification above the MLD becomes less
399 pronounced (Shi et al., 2018; Stünitz et al., 2020).

400 The modeled stress orientation is also compatible with seismological constraints.
401 The σ_{ss} indicates that the lower band above the MLD is dominated by slab-parallel
402 tension (Fig. 3G, K). In addition, the calculated T axes are generally aligned with the
403 local slab-parallel direction, matching the downdip-extensional stress pattern
404 commonly inferred for the lower planes of some double seismic zones (Sippl et al.,
405 2022). Together, these comparisons indicate that the MLD-bearing models capture
406 several first-order characteristics of the LSL, including its depth range, position relative
407 to the MLD, depth-dependent decrease in activity, and tensional stress state.

408 **4.3. Implications for the origin of the LSL**

409 The origin of the LSL is debated. Current mainstream explanations include the

antigorite dehydration embrittlement model (Jung et al., 2004; Mishra and Zhao, 2004; Peacock, 2001; Yamasaki and Seno, 2003), thermal stresses generated during slab bending and unbending (Goto et al., 1985; Hamaguchi et al., 1983), shear instabilities in dry olivine (John et al., 2009; Kelemen and Hirth, 2007), metastable phase transformations involving Al-rich orthopyroxene (Dera et al., 2013; Kirby et al., 1996), and more recently proposed metamorphic embrittlement related to orthopyroxene (Opx) reactions (Shi et al., 2022). The main points of contention concern the hydration state, degree of mechanical weakening, and stress conditions required for LSL formation and persistence.

The dehydration model has notable advantages, particularly in explaining the geometry of the DSZ (Peacock, 2001; Yamasaki and Seno, 2003) and is supported by extensive thermodynamic and experimental data (Jung et al., 2004; Peacock, 2003; Proctor and Hirth, 2015). For the LSL, however, uncertainties remain regarding the source and transport of H_2O to greater depths (Shi et al., 2022; Zhan, 2020). Furthermore, calculated antigorite dehydration fluxes do not consistently scale with the observed decay of seismicity with depth (fig. S6) (Barcheck et al., 2012). Many LSL regions are characterized by normal Vp/Vs values (Fig. 8A and fig. S7) (Wang et al., 2025) and are commonly inferred to represent relatively dry slab domains (Pennacchioni et al., 2020; Shi et al., 2022).

Some studies suggest that the LSL may represent a potential weakening zone within subducting slab mantle, where mechanical instability could arise through

processes such as shear instabilities (Kelemen and Hirth, 2007), metastable phase transformations (Dera et al., 2013; Kirby et al., 1996), and metamorphic reactions (Shi et al., 2022). However, it is important to note that weakened zones are associated with localized deformation (Wang et al., 2017), which cannot sustain differential stresses large enough to trigger seismic rupture (Dal Zilio et al., 2018). It therefore remains uncertain whether intrinsic weakening within the LSL can coexist with sufficiently high stress accumulation to initiate seismic rupture. Moreover, these weakening mechanisms are not expected to be restricted to oceanic subduction settings. In principle, they should also operate in continental subduction environments. Yet, a notable discrepancy is that well-developed double seismic zone structures are rarely observed in continental subduction systems (Brudzinski et al., 2007; Florez and Prieto, 2019; Sippl et al., 2022).

Our MLD-bearing models likely reconcile these misfits by offering a mechanical pathway for dry rupture. In our simulations, the MLD-bearing slab generates a lower band where a vast majority of particles exhibit high μ_{app}, overlapping the peak friction coefficient range required for dry peridotite seismic nucleation (Del Gaudio et al., 2009). Accordingly, our MLD-related framework can explain the LSL as a dry, peridotite-hosted seismic layer, which is more compatible with the observed Vp/Vs structure of some LSLs than an antigorite-rich interpretation (Fig. 8B). Meanwhile, in our model, the primary weakening zone is located within the MLD. This configuration promotes the concentration and amplification of differential stress within the high-strength LSL above the MLD, enabling stresses to build up to levels sufficient to exceed the failure

452 criterion and trigger seismic nucleation. In this framework, the LSL remains
453 mechanically strong and can maintain long-term compatibility with elevated
454 differential stress.

455 In our model, LSL formation is linked to the eclogitization of granulites within the
456 oceanic MLD (Fig. 9A). This mechanism is consistent with experimental constraints
457 on metamorphic reactions and rheological evolution during eclogitization: during
458 subduction, plagioclase and clinopyroxene in granulite progressively undergo prograde
459 reactions to form eclogite-facies minerals, including omphacite, garnet, and kyanite,
460 accompanied by the development of nanoscale reaction bands (Shi et al., 2018). These
461 ultrafine-grained products experience oriented growth and concurrent grain boundary
462 sliding (Massey et al., 2011), which collectively reduce rock strength and drive the
463 transition from dislocation creep to diffusion creep (McNamara et al., 2024). This
464 compositional layering and rheological weakening localize deformation within the
465 MLD and transfer stress to the overlying slab mantle section. This stress transfer
466 amplifies differential stress and raises μ_{app} above the MLD (Fig. 9B), allowing brittle
467 failure to occur in the lower band even without fluid-assisted or other processes induced
468 weakening (Del Gaudio et al., 2009; Toffol et al., 2022). As subduction proceeds and
469 grains grow to larger scales, the efficiency of diffusion creep decreases, the reaction
470 approaches completion, and rock strength is recovered, accompanied by a transition
471 back to dislocation creep (Stünitz et al., 2020). As a result, mantle viscosity increases
472 and differential stress decreases, while the Coulomb stress continues to increase with

depth. Consequently, the likelihood of brittle failure is reduced, and seismicity diminishes.

The stress localization and amplification associated with lithospheric layering may also operate in continental settings (Dal Zilio et al., 2019; Dal Zilio et al., 2018). For instance, when continental lithosphere undergoes delamination along a weak lower crustal layer or MLD (Wang and Kusky, 2019), stress is preferentially transferred to and concentrated within the surrounding stronger lithological layers, potentially generating intermediate-depth seismicity within the delaminating continental lithosphere (Cloetingh et al., 2004; Girbacea and Frisch, 1998; Kovács et al., 2021). Unlike oceanic lithosphere, however, continental downgoing slabs generally lack the dehydration reactions near the slab top that are critical for generating an upper seismic layer (Hacker et al., 2003; Kirby et al., 1996). Therefore, continental delamination is more likely to produce a single, predominantly dry seismic zone, analogous to the LSL in oceanic slabs, rather than a complete double seismic zone. This suggests that deformation localization associated with weak layers may provide a common mechanical framework for intermediate-depth seismicity in both oceanic and continental lithosphere, whereas well-developed double seismic zones are more likely to require hydrated oceanic slabs with suitable lithological architectures.

Given the complexity and diversity of lower seismicity zones, it is unlikely that any single mechanism can account for their full range of characteristics and regional variations worldwide (Florez and Prieto, 2019; Sippl et al., 2022; Zhan, 2020). A multi-

494 mechanism framework, in which different processes operate in concert and complement
495 one another, therefore appears to provide the most plausible explanation (Shi et al.,
496 2022; Zhan, 2020). Within this context, our model offers one potential end-member
497 scenario that may act in combination with other mechanisms to explain the observed
498 features of LSL. Although the mechanisms proposed for LSL formation are diverse,
499 they share a common mechanical requirement: rheological weakening coupled with
500 localized amplification of differential stress. Our results suggest that an oceanic MLD,
501 through its rheological layering during subduction, can establish an efficient structural
502 condition for concentrating and amplifying differential stress within the slab mantle
503 above it. In this sense, the MLD acts as a first-order mechanical control on rupture
504 localization within the lower seismic layer.
505

506 **5. Conclusion**

507 We developed 79 thermo-mechanical subduction models to investigate how
508 thermal- and composition- related rheological layering influences the formation of the
509 LSL in double seismic zones. By comparing models with and without an MLD across
510 different slab ages, and by analyzing the resulting viscosity structure, strain-rate
511 distribution, slab-parallel normal stress (σ_{ss}), and apparent friction coefficient (μ_{app}),
512 we suggest that eclogitization of granulites within the MLD provides a viable
513 mechanical explanation. Eclogitization-driven weakening localizes deformation within

514 the MLD and shifts stress to the slab mantle immediately above it, where differential
515 stress is amplified and the μ_{app} is elevated. As a result, the MLD-bearing models
516 develop a high-μ_{app} lower band above the MLD. This modeled band is consistent with
517 several first-order characteristics of the LSL, including its geometry, depth distribution,
518 tensional stress state, dry condition, and downward decrease in seismicity. These results
519 indicate that the oceanic MLD may exert a fundamental control on the formation of the
520 lower plane in some double seismic zones.

521 **CRediT authorship contribution statement**

522 Zhensheng Wang designed research; Tianyu Hu and Zhensheng Wang performed
523 research, analyzed data, and performed data interpretation; all co-authors wrote the
524 paper.

525 **Data and Materials Availability**

526 The numerical modeling code (Underworld2 v2.16.4) (Beucher et al., 2025) is
527 available at https://github.com/underworldcode/underworld2/releases. Earthquake
528 event data used in this study were obtained from the International Seismological Centre
529 (ISC) catalogue (Storchak et al., 2020) (https://doi.org/10.31905/D808B830). Seismic
530 velocity ratios (Vp/Vs) for peridotite were calculated using the Perple_X programs
531 (Connolly, 2005) (https://www.perplex.ethz.ch/) and thermodynamic parameters in
532 stx11 (Stixrude and Lithgow-Bertelloni, 2011). The Vp/Vs data for the Japan

subduction zone used in this study are from Wang et al. (2025).

Competing interests

The authors declare that they have no known competing financial interests or personal relationships that could have appeared to influence the work reported in this paper.

Acknowledgments

This study was supported by the National Natural Science Foundation of China (grants 42272243), National Key Research and Development Project of China (grants 2023YFF0804100) and the International Lithosphere Program (ILP). We gratefully acknowledge Prof. Dapeng Zhao and Dr. Jian Wang for kindly providing the observational Vp/Vs data for the Japan subduction zone used in this study.

References:

Barcheck, C.G., Wiens, D.A., van Keken, P.E. and Hacker, B.R., 2012. The relationship of intermediate- and deep-focus seismicity to the hydration and dehydration of subducting slabs. Earth and planetary science letters, 349-350: 153-160.

Benioff, H., 1949. Seismic evidence for the fault origin of oceanic deeps. Geological Society of America Bulletin, 60(12): 1837-1856.

Beucher, R. et al., 2025. Underworld2: Python Geodynamics Modelling for Desktop, HPC and Cloud. Zenodo.

Brudzinski, M.R., Thurber, C.H., Hacker, B.R. and Engdahl, E.R., 2007. Global Prevalence of Double Benioff Zones. Science, 316(5830): 1472-1474.

Capitanio, F.A. et al., 2025. Bridging the gap between subduction dynamics and the long-term strength of the Sunda megathrust. Nature Communications, 16(1): 10781.

Chen, K.X., Forsyth, D.W. and Fischer, K.M., 2024. A mid-lithospheric discontinuity detected beneath 155 Ma western Pacific seafloor using Sp receiver functions. Geophysical Research Letters, 51(5): e2024GL108347.

Cloetingh, S. et al., 2004. Thermo-mechanical controls on the mode of continental collision in the SE Carpathians (Romania). Earth and Planetary Science Letters, 218(1-2): 57-76.

Coble, R.L., 1963. A Model for Boundary Diffusion Controlled Creep in Polycrystalline Materials. Journal of Applied Physics, 34(6): 1679-1682.

Connolly, J.A., 2005. Computation of phase equilibria by linear programming: a tool for geodynamic modeling and its application to subduction zone decarbonation. Earth and Planetary Science Letters, 236(1-2): 524-541.

Dal Zilio, L., van Dinther, Y., Gerya, T. and Avouac, J.P., 2019. Bimodal seismicity in the Himalaya controlled by fault friction and geometry. Nature communications, 10(1): 48.

Dal Zilio, L., van Dinther, Y., Gerya, T.V. and Pranger, C.C., 2018. Seismic behaviour of mountain belts controlled by plate convergence rate. Earth and Planetary Science Letters, 482: 81-92.

Del Gaudio, P. et al., 2009. Frictional melting of peridotite and seismic slip. Journal of Geophysical Research: Solid Earth, 114(B6).

Dera, P. et al., 2013. Metastable high-pressure transformations of orthoferrosilite Fs82. Physics of the Earth and Planetary Interiors, 221: 15-21.

Florez, M.A. and Prieto, G.A., 2019. Controlling Factors of Seismicity and Geometry in Double Seismic Zones. Geophysical Research Letters, 46(8): 4174-4181.

Fujita, K. and Kanamori, H., 1981. Double seismic zones and stresses of intermediate depth earthquakes. Geophysical Journal International, 66(1): 131-156.

Gerya, T.V., Bercovici, D. and Becker, T.W., 2021. Dynamic slab segmentation due to brittle–ductile damage in the outer rise. Nature, 599(7884): 245-250.

Girbacea, R. and Frisch, W., 1998. Slab in the wrong place: lower lithospheric mantle delamination in the last stage of the Eastern Carpathian subduction retreat. Geology, 26(7): 611-614.

Goto, K., Hamaguchi, H. and Suzuki, Z., 1985. Earthquake generating stresses in a descending slab. Tectonophysics, 112(1-4): 111-128.

Hacker, B.R., Peacock, S.M., Abers, G.A. and Holloway, S.D., 2003. Subduction factory 2. Are intermediate-depth earthquakes in subducting slabs linked to metamorphic dehydration reactions? Journal of Geophysical Research: Solid Earth, 108(B1).

Hackston, A. and Rutter, E., 2016. The Mohr–Coulomb criterion for intact rock strength and friction–a re-evaluation and consideration of failure under polyaxial stresses. Solid Earth, 7(2): 493-508.

Hamaguchi, H., Goto, K. and Suzuki, Z., 1983. Double-planed structure of intermediatedepth seismic zone and thermal stress in the descending plate. Journal of Physics of the Earth, 31(6): 329-347.

Hirth, G. and Kohlstedt, D., 2003. Rheology of the upper mantle and the mantle wedge: A view from the experimentalists, pp. 83-105.

Huet, B., Yamato, P. and Grasemann, B., 2014. The Minimized Power Geometric model: An analytical mixing model for calculating polyphase rock viscosities consistent with experimental data. Journal of Geophysical Research: Solid Earth, 119(4): 3897-3924.

John, T. et al., 2009. Generation of intermediate-depth earthquakes by self-localizing thermal runaway. Nature Geoscience, 2(2): 137-140.

Jung, H., Green Ii, H.W. and Dobrzhinetskaya, L.F., 2004. Intermediate-depth earthquake faulting by dehydration embrittlement with negative volume change. Nature, 428(6982): 545-549.

Katsura, T., Yoneda, A., Yamazaki, D., Yoshino, T. and Ito, E., 2010. Adiabatic temperature profile in the mantle. Physics of the Earth and Planetary Interiors, 183(1-2): 212-218.

Katz, R.F., Spiegelman, M. and Langmuir, C.H., 2003. A new parameterization of hydrous mantle melting. Geochemistry, Geophysics, Geosystems, 4(9).

Kelemen, P.B. and Hirth, G., 2007. A periodic shear-heating mechanism for intermediate-depth earthquakes in the mantle. Nature, 446(7137): 787-790.

Kirby, S., Engdahl, R.E. and Denlinger, R., 1996. Intermediate-depth intraslab earthquakes and arc volcanism as physical expressions of crustal and uppermost mantle metamorphism in subducting slabs. Geophysical Monograph Series, 96: 195-214.

Kovács, I.J. et al., 2021. The 'pargasosphere'hypothesis: Looking at global plate tectonics from a new perspective. Global and Planetary Change, 204: 103547.

Kumar, P. and Kawakatsu, H., 2011. Imaging the seismic lithosphere-asthenosphere boundary of the oceanic plate. Geochemistry, Geophysics, Geosystems, 12(1).

Kylander-Clark, A.R.C. et al., 2007. Coupled Lu–Hf and Sm–Nd geochronology constrains prograde and exhumation histories of high- and ultrahigh-pressure eclogites from western Norway. Chemical geology, 242(1): 137-154.

Liu, M., Gerya, T.V., Li, Z.H., Chen, L. and Connolly, J.A., 2026. Deciphering grain-size reduction as a driver of mid-lithosphere discontinuity formation. Science Advances, 12(17): eaed4229.

Massey, M.A., Prior, D.J. and Moecher, D.P., 2011. Microstructure and crystallographic preferred orientation of polycrystalline microgarnet aggregates developed during progressive creep, recovery, and grain boundary sliding. Journal of Structural Geology, 33(4): 713-730.

McNamara, D.D., Wheeler, J., Pearce, M. and Prior, D.J., 2024. A key role for diffusion creep in eclogites: Omphacite deformation in the Zermatt-Saas unit, Italian Alps. Journal of Structural Geology, 179: 105033.

Mishra, O.P. and Zhao, D., 2004. Seismic evidence for dehydration embrittlement of the subducting Pacific slab. Geophysical research letters, 31(9).

Moresi, L., Dufour, F. and Mühlhaus, H.B., 2003. A Lagrangian integration point finite element method for large deformation modeling of viscoelastic geomaterials. Journal of computational physics, 184(2): 476-497.

Ohira, A. et al., 2017. Evidence for frozen melts in the mid-lithosphere detected from active-source seismic data. Scientific Reports, 7(1): 15770.

Peacock, S.M., 2001. Are the lower planes of double seismic zones caused by serpentine dehydration in subducting oceanic mantle? Geology, 29(4): 299.

Peacock, S.M., 2003. Thermal structure and metamorphic evolution of subducting slabs, pp. 7-22.

Pennacchioni, G. et al., 2020. Record of intermediate-depth subduction seismicity in a dry slab from an exhumed ophiolite. Earth and Planetary Science Letters, 548: 116490.

Proctor, B. and Hirth, G., 2015. Role of pore fluid pressure on transient strength changes and fabric development during serpentine dehydration at mantle conditions: Implications for subduction-zone

seismicity. Earth and Planetary Science Letters, 421: 1-12.
Ranalli, G., 1995. Rheology of the Earth. Springer Science & Business Media.
Rychert, C.A. et al., 2021. A dynamic lithosphere–asthenosphere boundary near the equatorial Mid-Atlantic Ridge. Earth and Planetary Science Letters, 566: 116949.
Rychert, C.A. and Shearer, P.M., 2011. Imaging the lithosphere-asthenosphere boundary beneath the Pacific using SS waveform modeling. Journal of Geophysical Research: Solid Earth, 116(B7).
Schmerr, N., 2012. The Gutenberg discontinuity: Melt at the lithosphere-asthenosphere boundary. Science, 335(6075): 1480-1483.
Schmidt, M.W. and Poli, S., 1998. Experimentally based water budgets for dehydrating slabs and consequences for arc magma generation. Earth and Planetary Science Letters, 163(1-4): 361-379.
Seton, M. et al., 2020. A global data set of present-day oceanic crustal age and seafloor spreading parameters. Geochemistry, Geophysics, Geosystems, 21(10): e2020GC009214.
Shi, F. et al., 2018. Lower-crustal earthquakes in southern Tibet are linked to eclogitization of dry metastable granulite. Nature communications, 9(1): 3483.
Shi, F. et al., 2022. Metamorphism-facilitated faulting in deforming orthopyroxene: Implications for global intermediate-depth seismicity. Proceedings of the National Academy of Sciences, 119(11): e2112386119.
Shinevar, W.J., Behn, M.D. and Hirth, G., 2015. Compositional dependence of lower crustal viscosity. Geophysical Research Letters, 42(20): 8333-8340.
Sippl, C., Dielforder, A., John, T. and Schmalholz, S.M., 2022. Global constraints on intermediate-depth intraslab stresses from slab geometries and mechanisms of double seismic zone earthquakes. Geochemistry, Geophysics, Geosystems, 23(9): e2022GC010498.
Sizova, E., Gerya, T., Brown, M. and Perchuk, L.L., 2010. Subduction styles in the Precambrian: Insight from numerical experiments. Lithos, 116(3-4): 209-229.
Skora, S. et al., 2009. The duration of prograde garnet crystallization in the UHP eclogites at Lago di Cignana, Italy. Earth and Planetary Science Letters, 287(3-4): 402-411.
Stixrude, L. and Lithgow-Bertelloni, C., 2011. Thermodynamics of mantle minerals-II. Phase equilibria. Geophysical Journal International, 184(3): 1180-1213.
Storchak, D.A. et al., 2020. Rebuild of the Bulletin of the International Seismological Centre (ISC)—part 2: 1980–2010. Geoscience Letters, 7(1): 18.
Stünitz, H. et al., 2020. Transformation weakening: Diffusion creep in eclogites as a result of interaction of mineral reactions and deformation. Journal of Structural Geology, 139: 104129.
Tharimena, S., Rychert, C., Harmon, N. and White, P., 2017. Imaging Pacific lithosphere seismic discontinuities—Insights from SS precursor modeling. Journal of geophysical research. Solid earth, 122(3): 2131-2152.
Toffol, G., Yang, J., Pennacchioni, G., Faccenda, M. and Scambelluri, M., 2022. How to quake a subducting dry slab at intermediate depths: Inferences from numerical modelling. Earth and Planetary Science Letters, 578: 117289.
Tosi, N., Yuen, D.A., de Koker, N. and Wentzcovitch, R.M., 2013. Mantle dynamics with pressure-and temperature-dependent thermal expansivity and conductivity. Physics of the Earth and Planetary Interiors, 217: 48-58.
Turcotte, D.L. and Schubert, G., 2002. Geodynamics. Cambridge university press.

683 Ulmer, P. and Trommsdorff, V., 1995. Serpentine Stability to Mantle Depths and Subduction-Related
684 Magmatism. Science, 268(5212): 858-861.
685 Wang, D. et al., 2022. Mantle Wedge Water Contents Estimated From Ultrasonic Laboratory
686 Measurements of Olivine-Antigorite Aggregates. Geophysical Research Letters, 49(10):
687 e2022GL098226.
688 Wang, J. et al., 2025. Seismic Evidence for Large-Scale Intraslab Heterogeneity Beneath Northeast Japan.
689 Journal of Geophysical Research: Solid Earth, 130(4): e2024JB030046.
690 Wang, Y. et al., 2017. A laboratory nanoseismological study on deep-focus earthquake micromechanics.
691 Science Advances, 3(7): e1601896.
692 Wang, Z. and Kusky, T.M., 2019. The importance of a weak mid-lithospheric layer on the evolution of
693 the cratonic lithosphere. Earth-Science Reviews, 190: 557-569.
694 Xiang, G., Wang, Z. and Kusky, T.M., 2021. Density and viscosity changes between depleted and
695 primordial mantle at ~1000 km depth influence plume upwelling behavior. Earth and Planetary
696 Science Letters, 576: 117213.
697 Yamasaki, T. and Seno, T., 2003. Double seismic zone and dehydration embrittlement of the subducting
698 slab. Journal of Geophysical Research: Solid Earth, 108(B4).
699 Zhan, Z., 2020. Mechanisms and Implications of Deep Earthquakes. Annual Review of Earth and
700 Planetary Sciences, 48(1): 147-174.
701 Zhang, H.L., Ravat, D. and Lowry, A.R., 2020. Crustal composition and Moho variations of the central
702 and eastern United States: Improving resolution and geologic interpretation of EarthScope USArray
703 seismic images using gravity. Journal of Geophysical Research: Solid Earth, 125(3): e2019JB018537.

704

705

706 **Figure Captions**

707 **Fig. 1. Distribution of DSZs and oceanic MLDs, and their depth relationships.**

708 **(A)** Distribution of oceanic MLDs and DSZs in the Pacific region. Circles denote
709 oceanic MLDs (Tharimena et al., 2017) and quadrilaterals indicate DSZ regions (Florez
710 and Prieto, 2019; Sippl et al., 2022). Background colors show oceanic age (Seton et al.,
711 2020). **(B)** Probability-density distributions of depth from the slab top for oceanic
712 MLDs and LSLs (Florez and Prieto, 2019; Tharimena et al., 2017). **(C)** Vertical cross

713 section of subduction zone near Japan (lower right) and distribution of earthquakes.
714 Black circles denote earthquakes; the blue dashed line marks the slab top and bottom,
715 and the red band represents the MLD.

716 **Fig. 2. Initial model setup and effects of parameter variations on mantle**
717 **rheology. (A)** Initial temperature field. **(B)** Initial material field without MLD. **(C)**
718 Initial material field including residual-melt–derived granulites. **(D)** Initial material
719 field including both residual-melt–derived and intrusive-melt–derived granulites. **(E)**
720 Temperature profile at x = 1450 km. **(F)** Density profiles of peridotite (black) and
721 mafic lithologies (green; oceanic crust, granulite, and eclogite) along the mantle
722 adiabat. **(G)** Viscosity profiles. Black, purple, and green lines denote the viscosity
723 profiles of Group 1 (No MLD), Group 2 (Residual), and Group 3 (Residual +
724 Intrusive), respectively. **(H)** Different modeling scenarios for diffusion creep of
725 eclogites with varying characteristic timescale (t_{trans}). **(I)** Different modeling
726 scenarios for diffusion creep of eclogites with varying minimum viscosity following
727 eclogitization (η_{min}).

728 **Fig. 3. Representative snapshots of the three model groups (η_{min}=1e^{18} Pa·s;**
729 **t_{trans}=30 Myr; Slab age = 70 Myr).** From left to right: Group 1 (No MLD), Group 2
730 (Residual), and Group 3 (Residual + Intrusive). **(A, E, I)** Viscosity field, with the brown
731 dashed line marking the 1350°C isotherm. Black lines denote the oceanic crust, red
732 lines denote residual eclogite/granulite, and purple lines denote intrusive
733 eclogite/granulite. The green dashed line represents the eclogitization boundary (Zhang

et al., 2020). **(B, F, J)** Strain rate field. **(C, G, K)** Distribution of the slab-parallel normal stress (σ_{ss}), with the orange dashed line indicating the antigorite dehydration boundary (Ulmer and Trommsdorff, 1995). The gray shaded region indicates the oceanic MLD. Light blue short lines indicate the calculated T axes. **(D, H, L)** Distribution of the apparent friction coefficient (μ_{app}).

Fig. 4. Distribution of the apparent friction coefficient (μ_{app}) in models with different slab ages. From left to right: Group 1 (No MLD), Group 2 (Residual), and Group 3 (Residual + Intrusive). From top to bottom: models with increasing slab ages. The orange dashed line indicates the antigorite dehydration boundary (Ulmer and Trommsdorff, 1995). The gray shaded region indicates the oceanic MLD.

Fig. 5. Distribution of the apparent friction coefficient (μ_{app}) for combined residual and intrusive MLD models. Panels show results for varying minimum viscosity after eclogitization (η_{min} = 10^{18}–10^{22} Pa·s) and the characteristic timescales (t_{trans} = 5–30 Myr).

Fig. 6. Variation of apparent friction coefficient (μ_{app}) with the depth from the slab top. Red, orange, and blue points denote different model groups: No MLD, Residual, and Residual + Intrusive models, respectively. Gray shaded regions mark the oceanic crust and MLD depth ranges. Black dashed lines indicate μ_{app} = 0.4 and 0.7. The interval between these two values corresponds to conditions under which earthquakes may nucleate in dry peridotite (Del Gaudio et al., 2009), whereas values below 0.4 correspond to conditions favorable for earthquake nucleation in wet

peridotite.

Fig. 7. Comparison between model results and seismic observations. (A) Comparison of depth from the slab top for observed oceanic MLDs, observed LSLs, and model-predicted high-μ_{app} lower bands for groups with MLD (orange band) and no MLD (gray band). Open symbols denote oceanic MLD or other discontinuities, including red open circles from Tharimena et al. (2017), green open squares from Rychert and Shearer (2011), orange open diamonds from Kumar and Kawakatsu (2011), and gray open inverted triangles from Schmerr (2012). Solid circles represent observed LSL depth from the slab top, with blue points from Florez and Prieto (2019), green points from Brudzinski et al. (2007). **(B)** Depth distribution of lower-plane earthquakes in Japan. **(C)** Probability-density distributions of model particles with $\mu_{app} > 0.4$ in MLD-bearing models for subducting slabs of different ages.

Fig. 8. Seismic Vp/Vs constraints on the origin of the LSL beneath Japan. (A) Vertical cross section at 39.6°N and 140°–142.5°E showing the depth distribution of earthquakes from 2000 to 2020. Black circles denote earthquakes. Background colors denote the Vp/Vs along the same profile (from Wang et al. (2025)). **(B)** Vp/Vs values at the locations of earthquakes within the LSL beneath Japan (fig. S7), compared with experimental Vp/Vs values of antigorite and peridotite under different pressures. The Vp/Vs curve for peridotite is calculated using Perple_X (Connolly, 2005) based on the thermodynamic parameters in stx11 (Stixrude and Lithgow-Bertelloni, 2011). The Vp/Vs curve for antigorite is from Wang et al. (2022).

Fig. 9. Schematic illustration of the mechanism for LSL formation. The green dashed line represents the eclogitization boundary (Zhang et al., 2020). (A) The continuous band represents the MLD derived from residual melts, while scattered ellipsoids represent intrusive MLD bodies. The transition from purple to cyan regions illustrates the progressive eclogitization of metastable granulites within the MLD. Orange circles represent seismicity. The thin red band above the MLD indicates LSL, whereas the thin blue band indicates USL. (B) Conceptual model showing the relationship between slab age, MLD depth, and the distribution of apparent friction coefficient μ_{app} during subduction. The blue shaded region indicates the typical MLD depth range. Schematic vertical μ_{app} profiles show two high-μ_{app} bands: an upper band near the oceanic crust, corresponding to the USL, and a lower band immediately above the MLD, corresponding to the predicted LSL. The high-μ_{app} lower band follows the top of the MLD as slab age increases. Note that both the USL and LSL can only develop during subduction. The relationships shown here are intended solely to illustrate their variations with slab age and do not represent the actual geometry or morphology of subducting slabs.

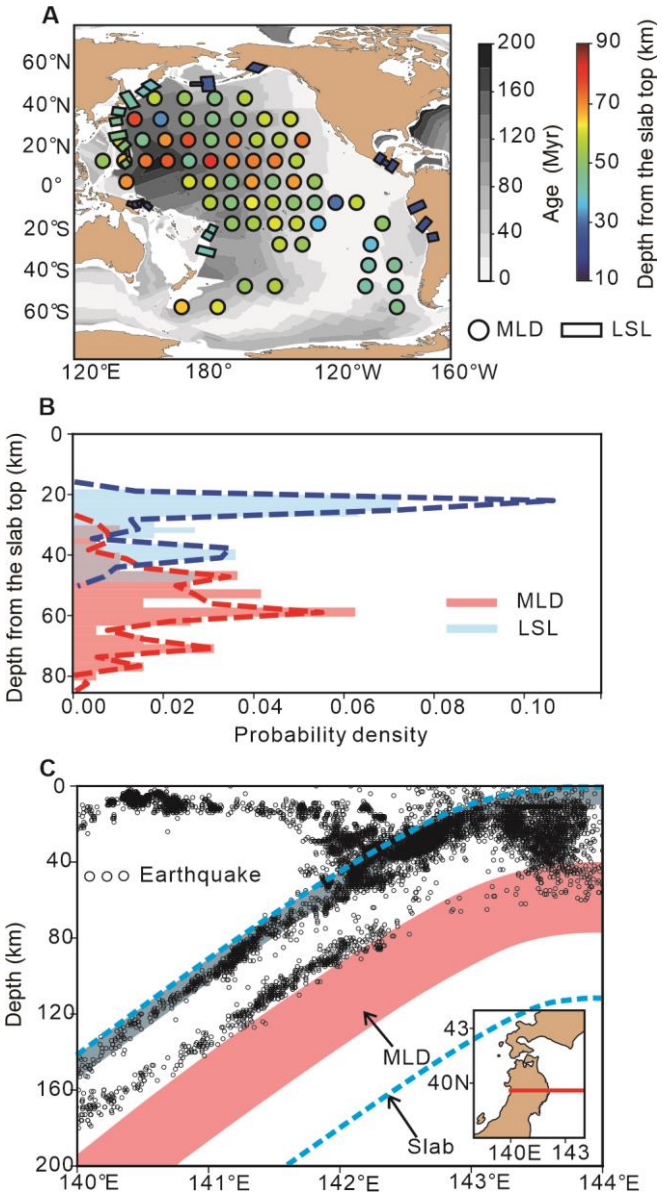

794

795 **Figure1**

796

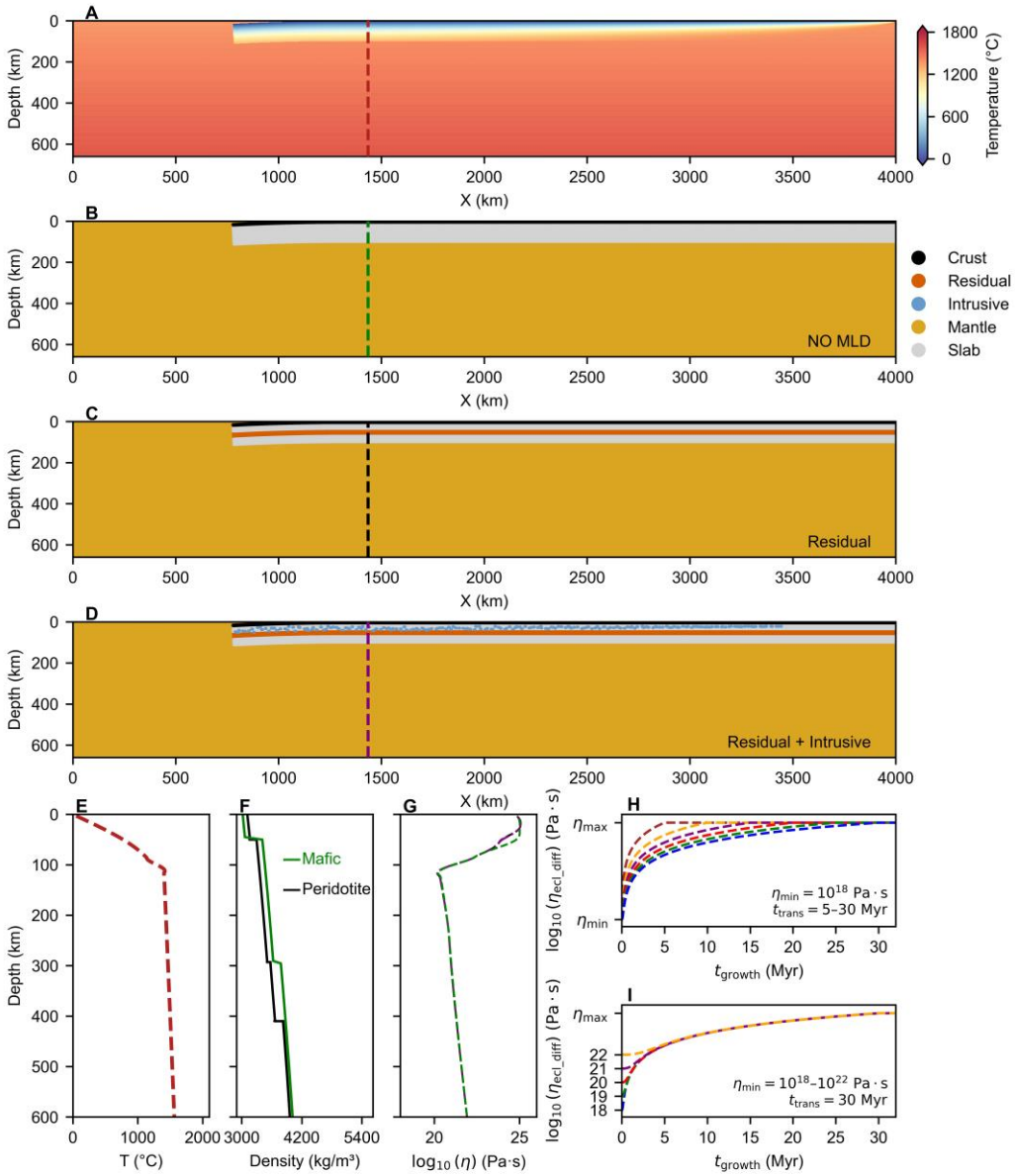

797

798 **Figure2**

799

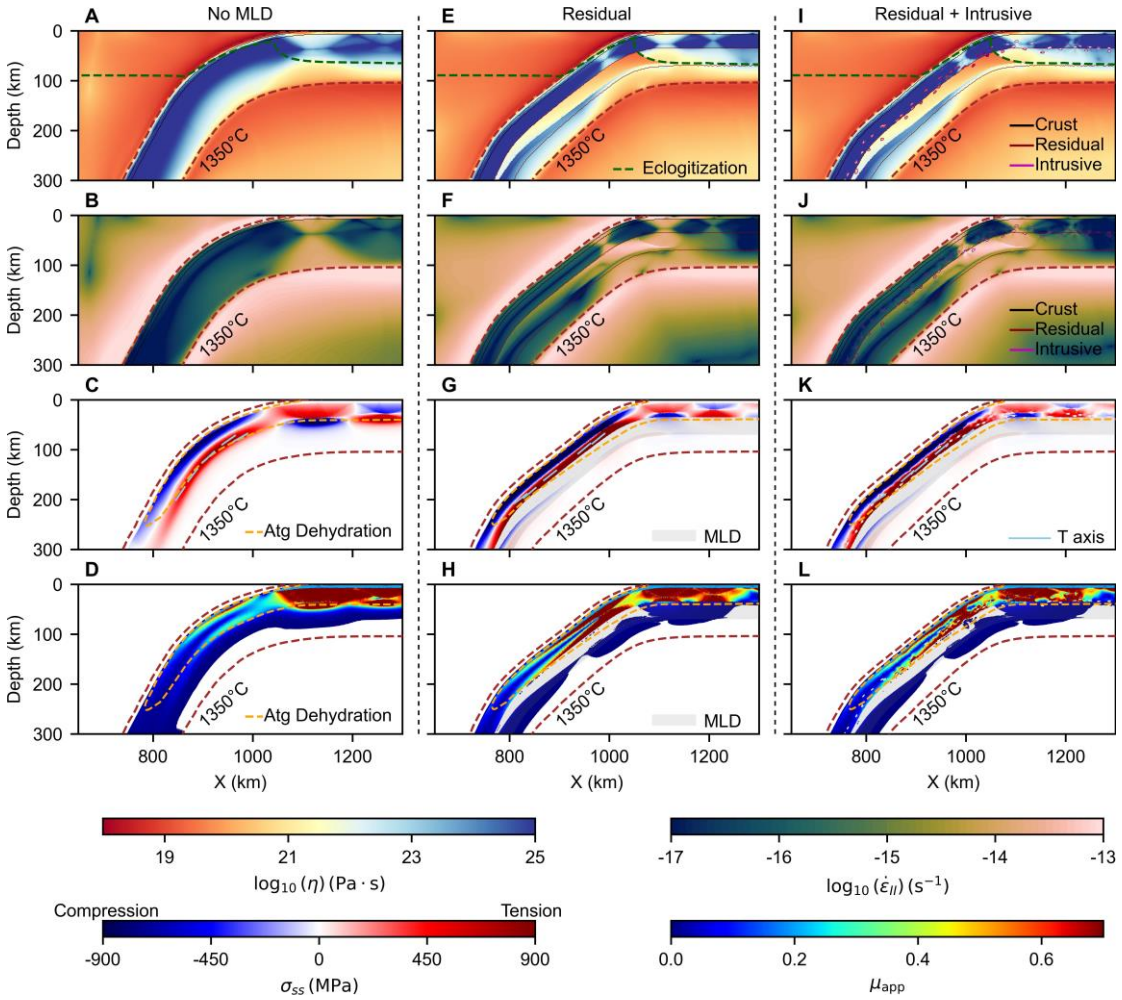

800

801 **Figure3**

802

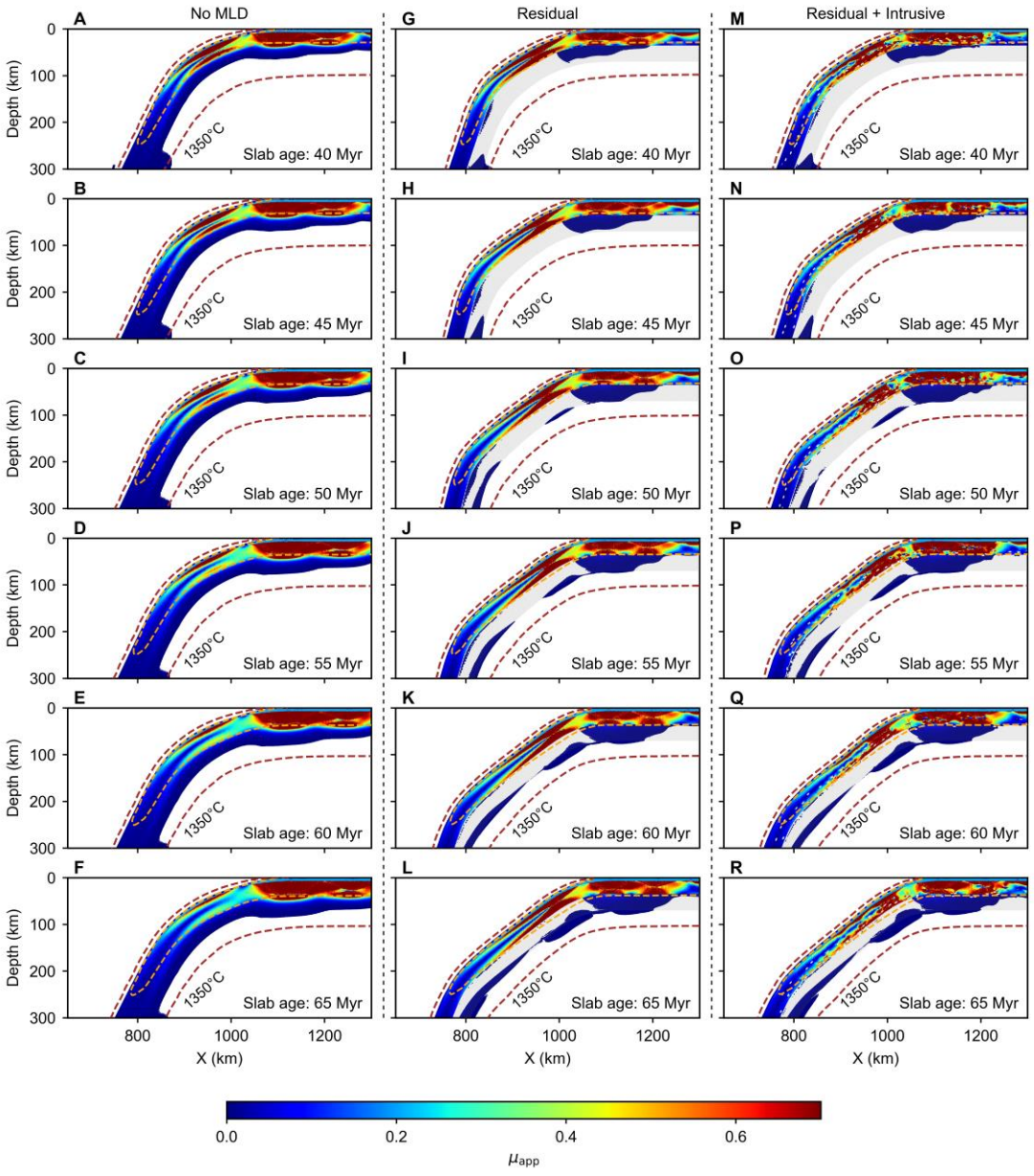

803

804 **Figure4**

805

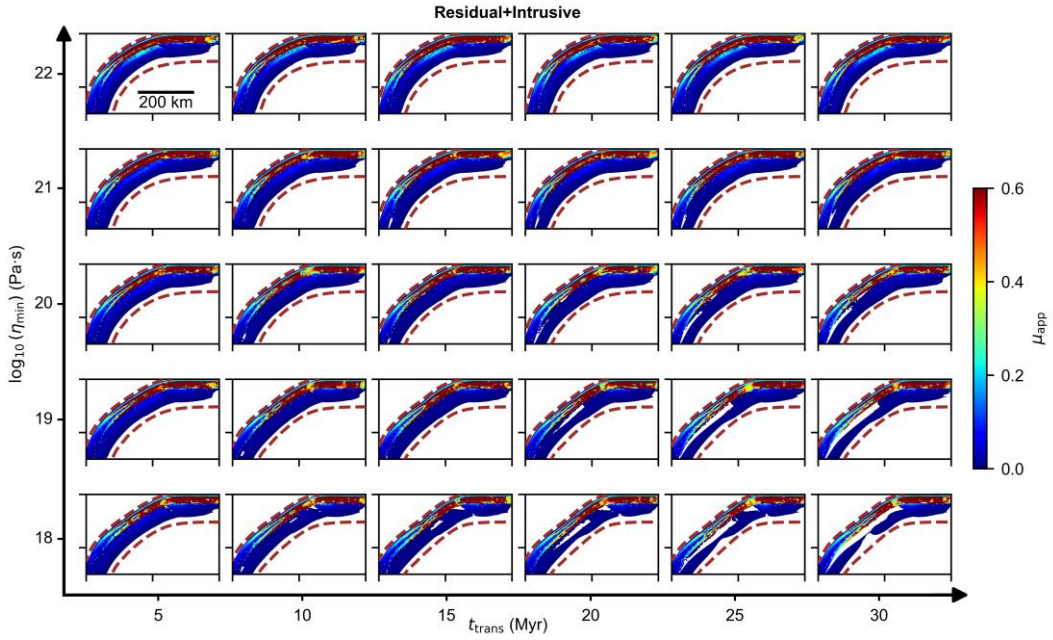

806

807 **Figure5**

808

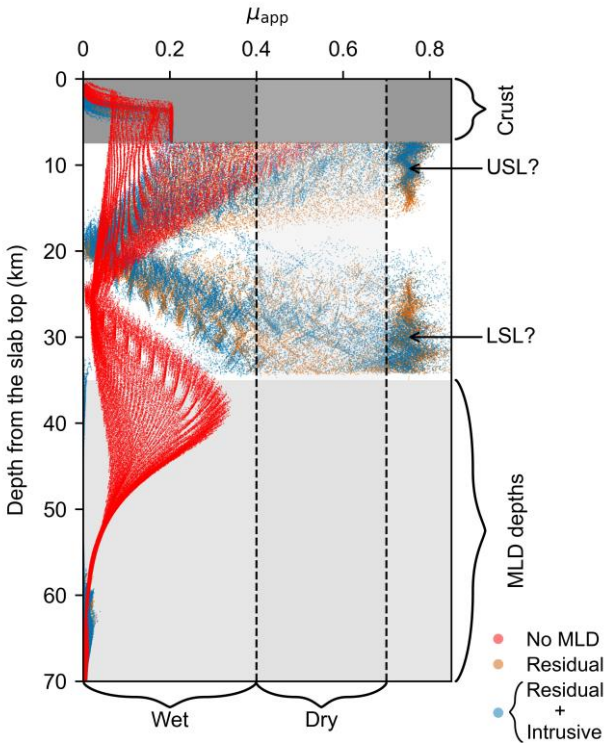
μ_{app}
0
0.2
0.4
0.6
0.8
Depth from the slab top (km)
0
10
20
30
40
50
60
70
Crust
USL?
LSL?
MLD depths
Wet
Dry
No MLD
Residual
Residual + Intrusive

Figure6

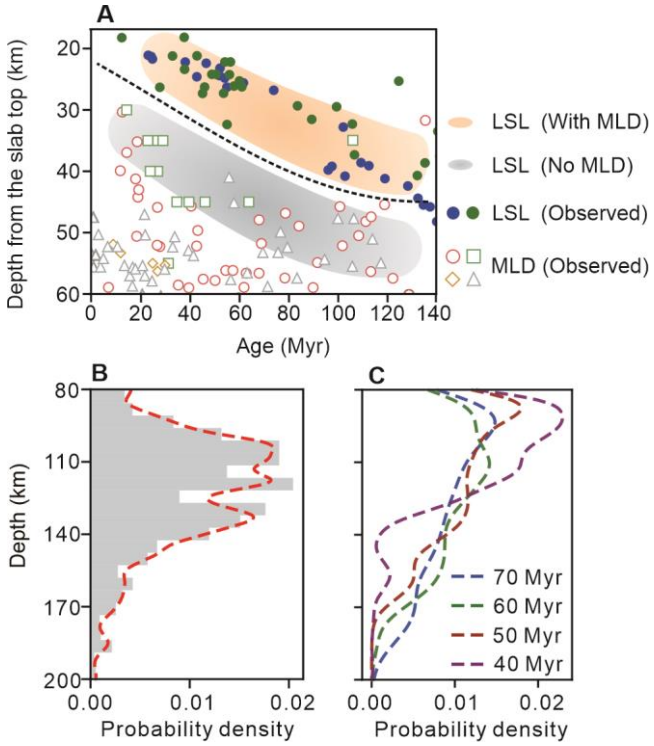

812

813 **Figure7**

814

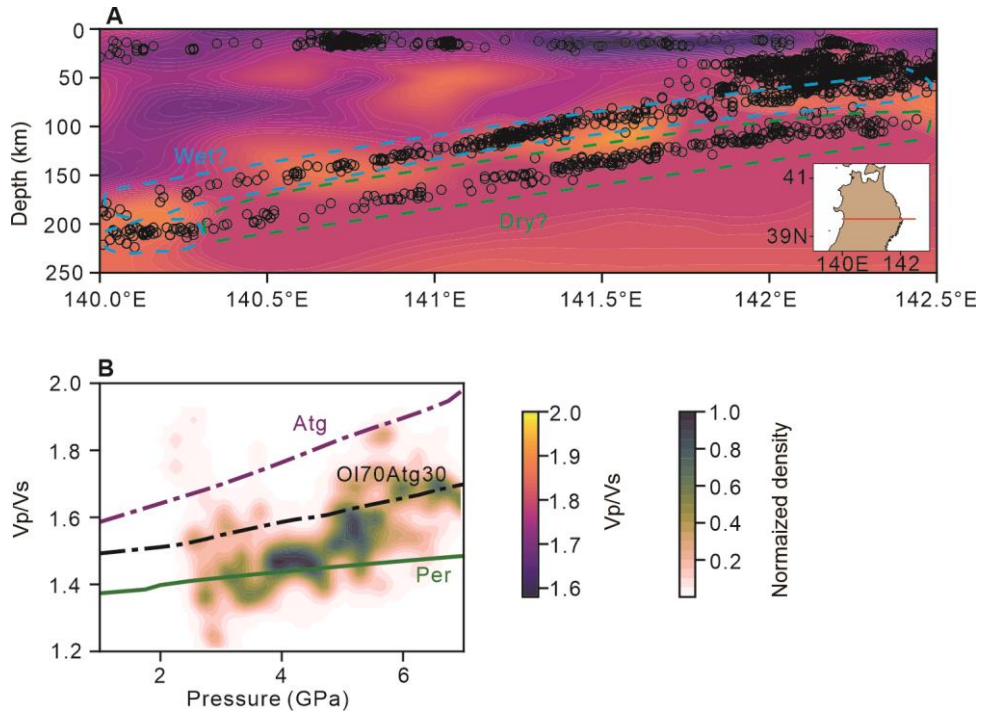

815

816 **Figure8**

817

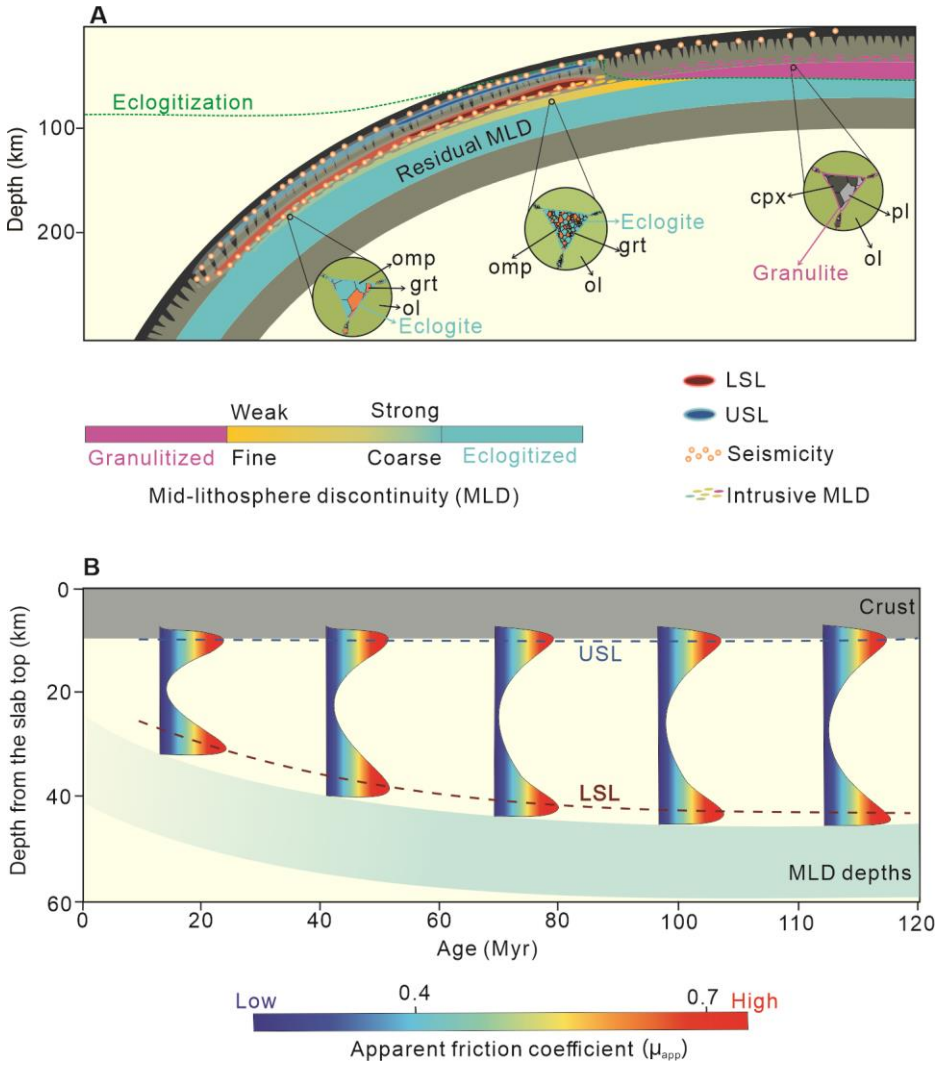

818

819 **Figure9**

Supplementary Materials for

Linking double seismic zones to oceanic lithosphere rheological layering: the role of mid-lithospheric discontinuities

Tianyu Hu[1], Zhensheng Wang[1]*, Junfeng Zhang[1]*, Feng Shi[1], Fabio Capitanio[1,2], Xinnuo Li[1], Sierd Cloetingh[3,4], István J. Kovács[3], Alessio Lavecchia[3,5,4], Alexander Koptev[6,3]

Corresponding author: Zhensheng Wang (Email: jasonwang@cug.edu.cn); Junfeng Zhang (Email: jfzhang@cug.edu.cn)

The PDF file includes:

Figs. S1 to S7
Tables S1 to S4
References

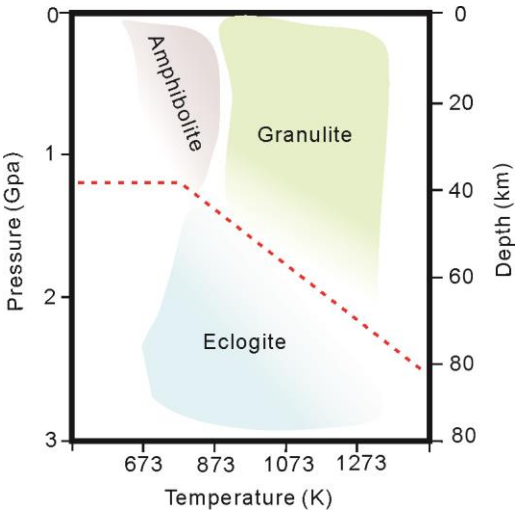

Fig. S1. Schematic phase diagram. The relationships between granulite-facies rocks and other lithologies (modified from Shi et al. (2018)). The red dashed line marks the phase boundary from garnet granulite to eclogite (Zhang et al., 2020).

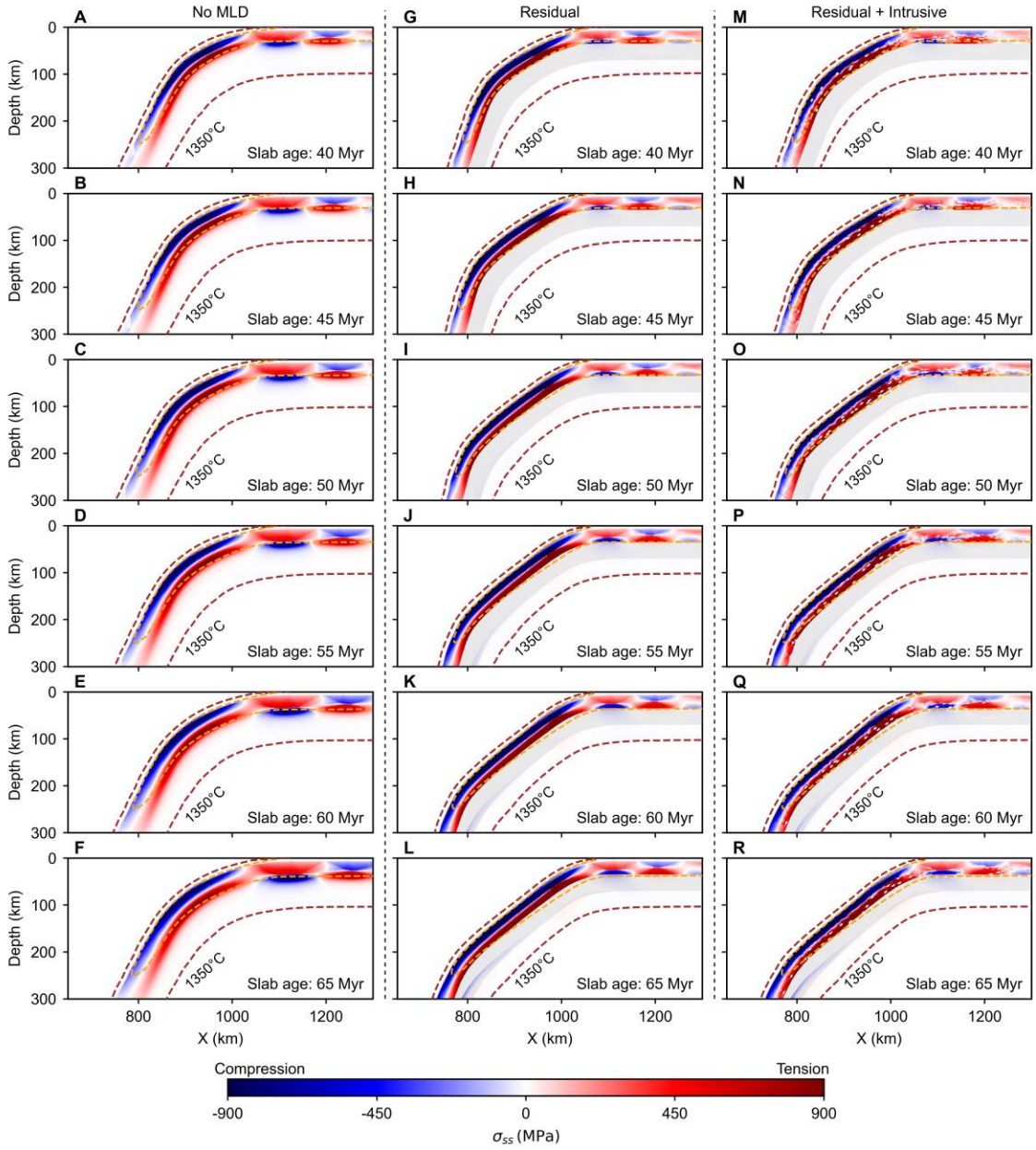

32

33 **Fig. S2. Distribution of the σ_{ss} in models with different slab ages.** From left to right:

34 Group 1 (No MLD), Group 2 (Residual), and Group 3 (Residual + Intrusive). From top to bottom,

35 models with increasing slab ages. The orange dashed line indicates the antigorite dehydration

36 boundary (Ulmer and Trommsdorff, 1995). The gray shaded region indicates the oceanic MLD.

37

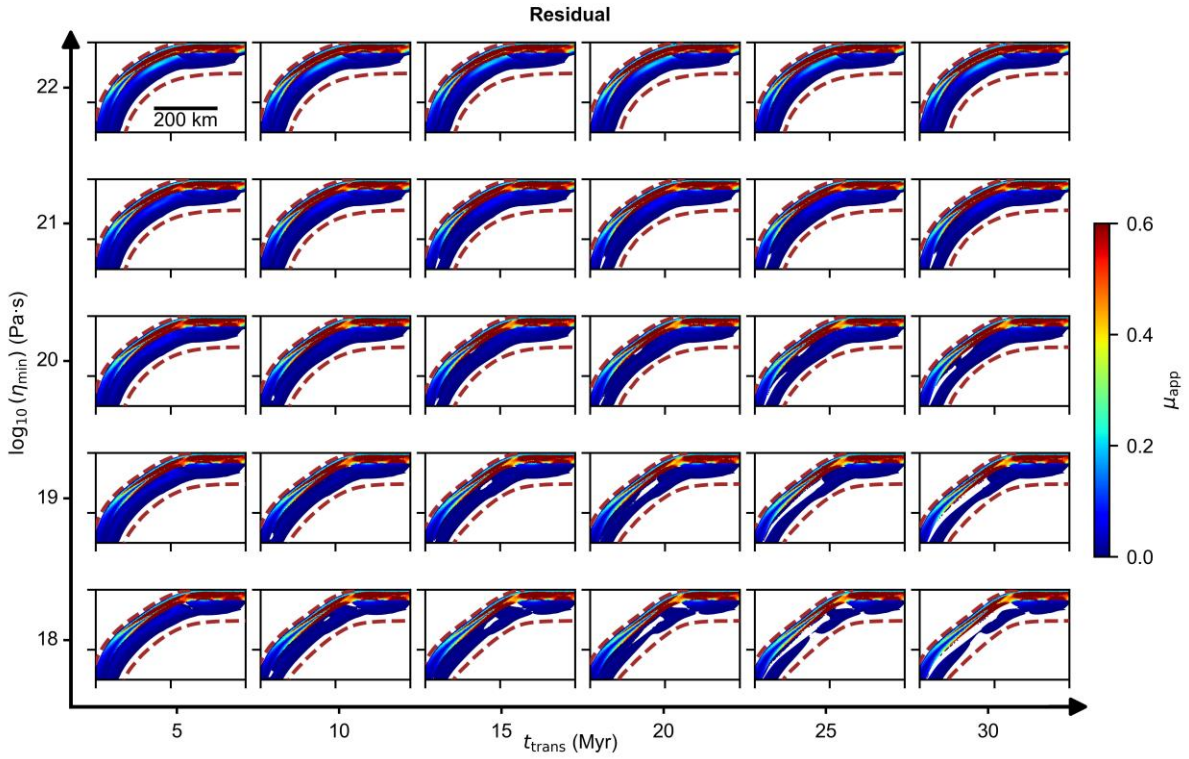

Fig. S3. Distribution of the apparent friction coefficient (μ_{app}) for residual MLD models.

Panels show results for varying the minimum viscosity following eclogitization (η_{min} = 10^{18}–10^{22} Pa·s) and the characteristic timescale (t_{trans} = 5–30 Myr).

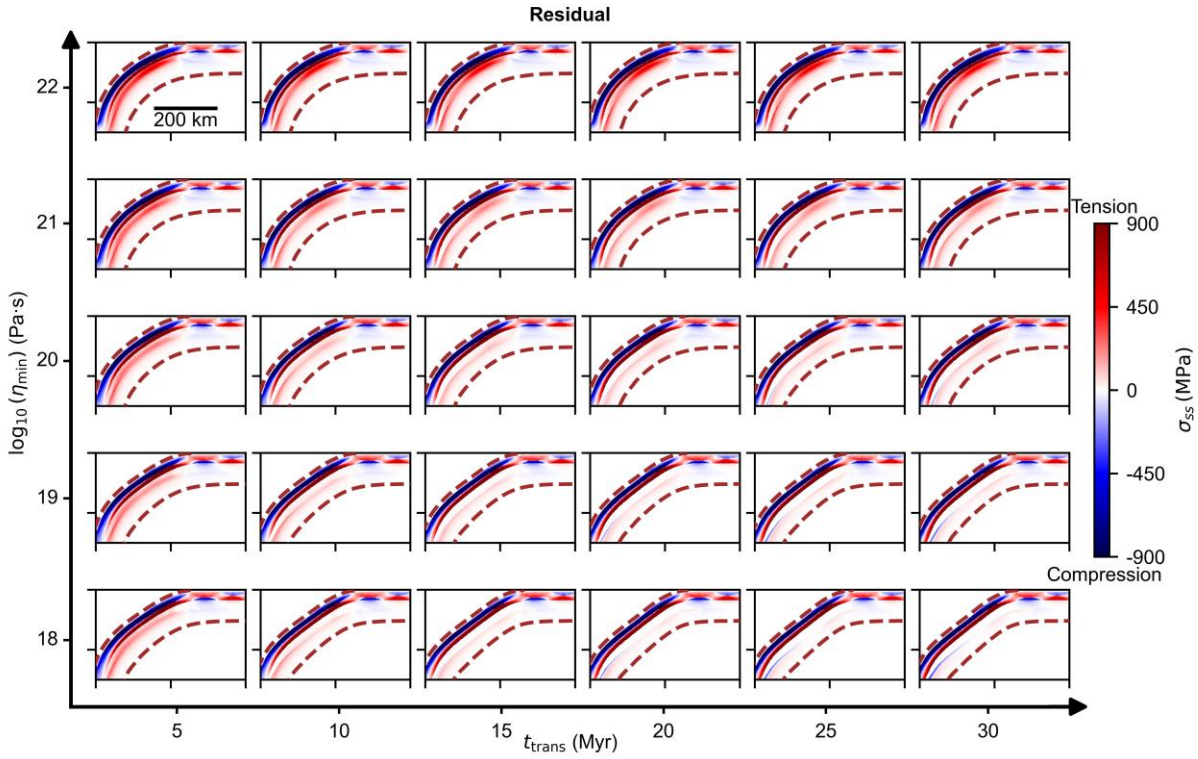

43

44 **Fig. S4. σ_{ss} distributions for residual MLD models.** Panels show results for varying the

45 minimum viscosity following eclogitization (η_{min} = 10^{18}–10^{22} Pa·s) and the characteristic

46 timescale (t_{trans} = 5–30 Myr).

47

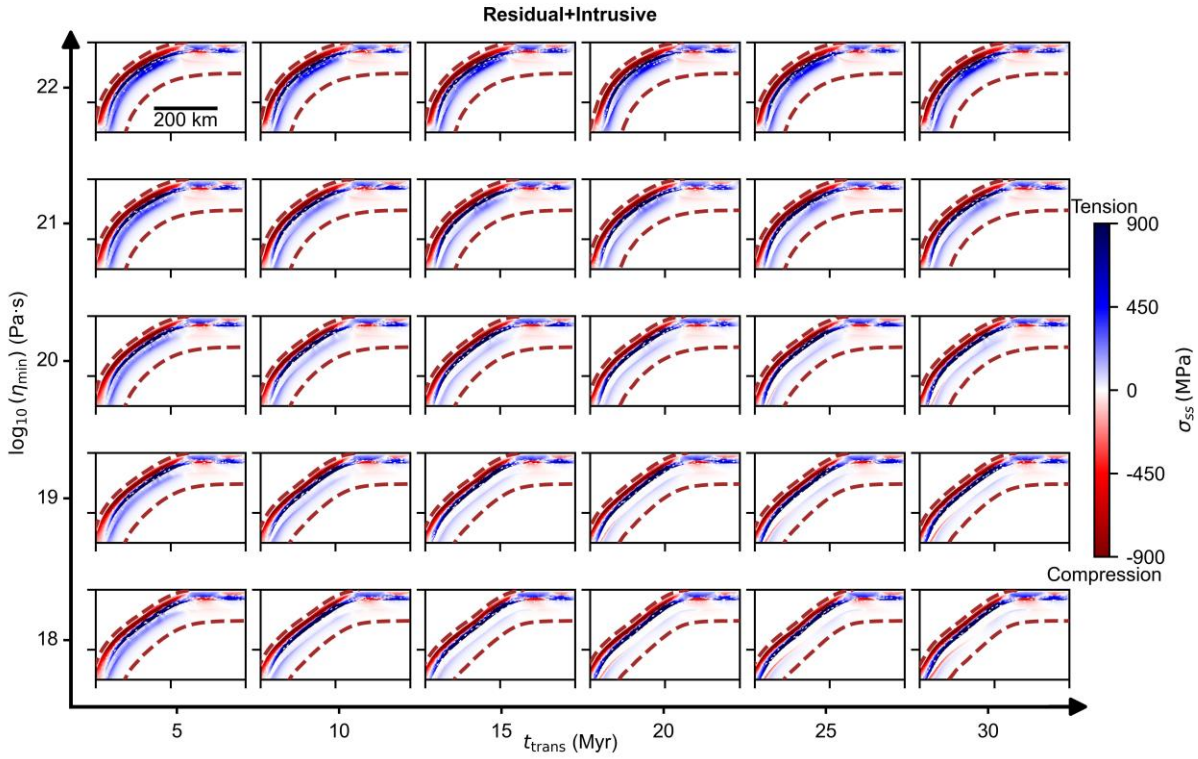

Fig. S5. σ_{ss} distributions for combined residual and intrusive MLD models. Panels show results for varying the minimum viscosity following eclogitization (η_{min} = 10^{18}–10^{22} Pa·s) and the characteristic timescale (t_{trans} = 5–30 Myr).

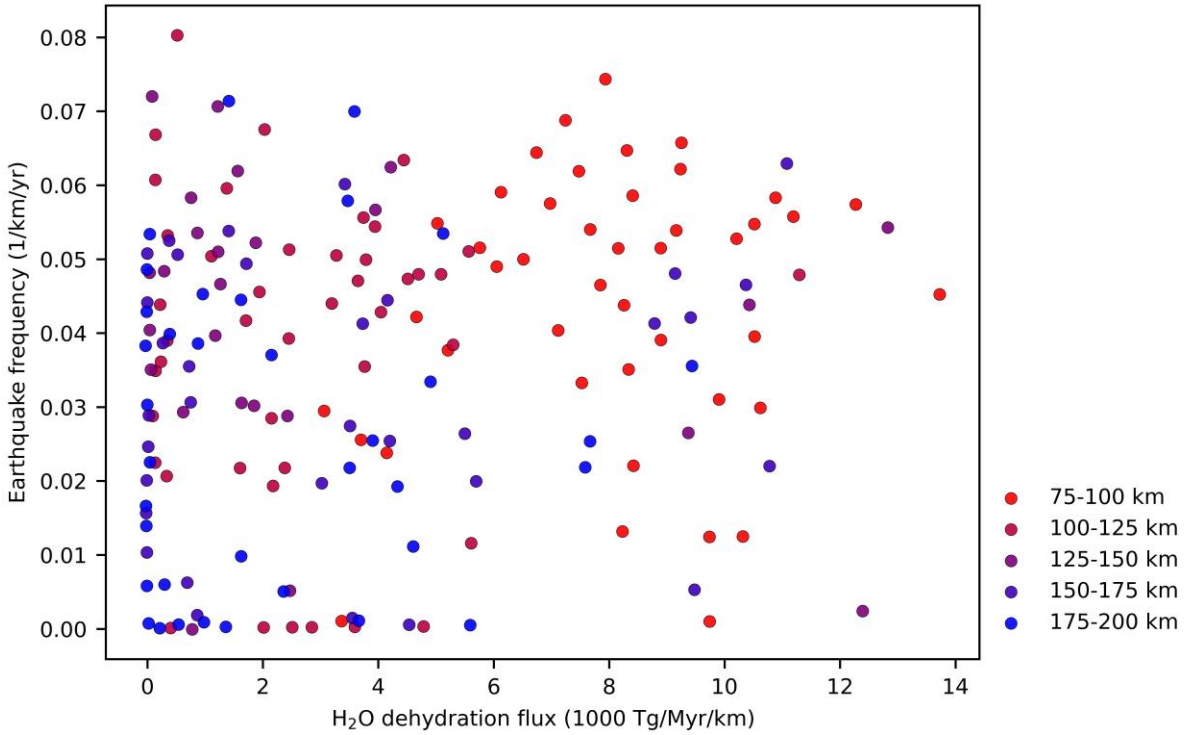

Fig. S6. Correlation between earthquake frequency and dehydration flux. Earthquake frequency plotted against dehydration flux along the trench within the depth range of 75–200 km.

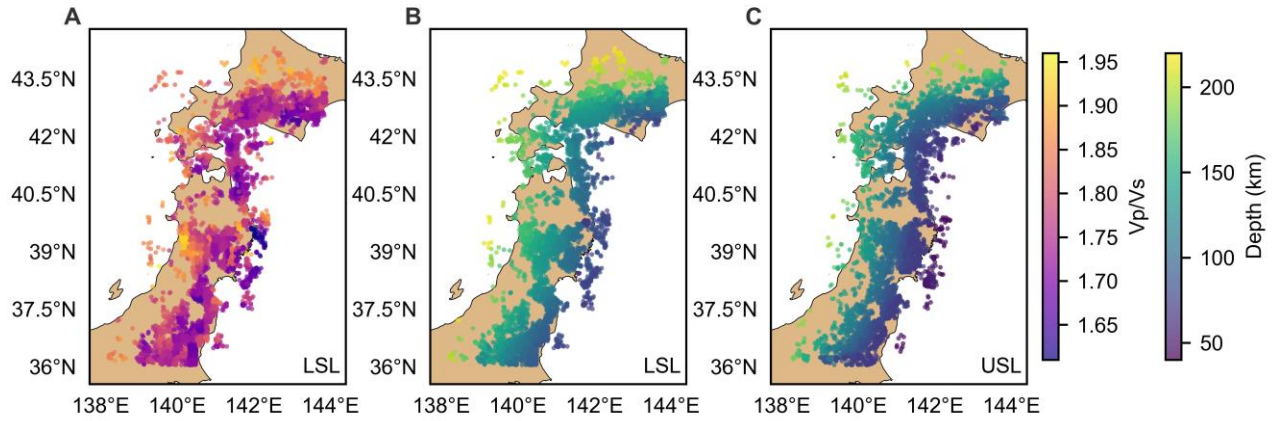

58

59 **Fig. S7. Depths and corresponding Vp/Vs ratios of intermediate-depth earthquakes in the**

60 **Japanese region. (A)** Vp/Vs ratios for earthquakes within the Lower Seismic Layer (LSL). **(B)**

61 Depths of earthquakes within the LSL. **(C)** Depths of earthquakes within the Upper Seismic Layer

62 (USL). Earthquakes data are from International Seismological Centre (Bondár and Storchak, 2011;

63 Storchak et al., 2017; Storchak et al., 2020). Vp/Vs data from (Wang et al., 2025).

64

Table S1. Model parameters.

Symbol	Meaning	Value	Units
A	Pre-exponential parameter of flow law	See in Table S3	$Pa^{-n}·s^{-1}$
E^*	Activation energy of flow law	See in Table S3	$J·mol^{-1}$
V^*	Activation volume of flow law	See in Table S3	$m^3·mol^{-1}$
n	Power-law exponent of flow law	See in Table S3	-
C_1	Friction coefficient	See in Table S3	-
C_0	Cohesion	See in Table S3	Pa
P	Hydrostatic pressure	-	Pa
R	Gas constant	8.314	$J·K^{-1}·mol^{-1}$
T	Temperature	-	K
η	Viscosity	-	Pa s
η_{min}	Minimum viscosity for eclogite diffusion creep	$10^{18\text{-}22}$	Pa s
η_{max}	Maximum viscosity for eclogite diffusion creep	10^{25}	Pa s
η_{min_model}	Model minimum viscosity	10^{18}	Pa s
η_{max_model}	Model maximum viscosity	10^{25}	Pa s
$\dot{\varepsilon}_{II}$	Second invariant of the strain rate	-	s^{-1}
κ	Thermal conductivity	-	$W·m^{-1}·K^{-1}$
g	Gravitational acceleration	9.8	$m·s^{-2}$
ρ_{depth_per}	Reference density of peridotite along mantle adiabat	Fig. 2F	$kg·m^{-3}$
ρ_{depth_mafic}	Reference density of oceanic crust / granulite / eclogite along mantle adiabat	Fig. 2F	$kg·m^{-3}$
C_p	Specific heat	1300	$J·kg^{-1}·K^{-1}$
α	Thermal expansion coefficient	-	K^{-1}
T_p	Mantle potential temperature	1350	℃
k_{410}	Clapeyron slope 410 km phase transition	1.5	$MPa·K^{-1}$
k_{660}	Clapeyron slope 660 km phase transition	-0.5	$MPa·K^{-1}$
c	Volume fraction of granulite/eclogite	0.0-0.04	-

Table S2. Parameters for thermal expansion coefficient (α) and thermal conductivity (κ) of crust and mantle materials (Tosi et al., 2013).

	Upper mantle	MTZ	Units
a_0	3.15×10^{-5}	2.84×10^{-5}	K^{-1}
a_1	1.02×10^{-8}	6.49×10^{-9}	K^{-2}
a_2	-0.76	-0.88	K
a_3	3.63×10^{-2}	2.61×10^{-2}	GPa^{-1}
d_0	2.47	3.81	$W \cdot m^{-1} \cdot K^{-1}$
d_1	0.33	0.34	$W \cdot m^{-1} \cdot K^{-1} \cdot GPa^{-1}$
d_2	0.48	0.56	

Table S3. Rheology parameters for the deformation mechanisms of crust and mantle material. The parameters for the upper mantle, mantle transition zone, and crust are based on van Hunen and van den Berg (2008). Eclogite parameters are based on Zhang and Green (2007), granulite parameters are based on Wang et al. (2012), activation volume values are taken from Farla et al. (2017), with pressure corrections included.

	Mechanism	A ($Pa^{-n}\ s^{-1}$)	n	E^* (J/mol)	V^* (cm^3/mol)	C_1	C_0 (Pa)
Crust	disl	8.8×10^{-25}	3.4	2.60×10^5	10	0.2	1.0×10^7
MLD-Eclogite	disl / diff*	2.26×10^{-17}	3.5	4.70×10^5	5	0.6	1.0×10^7
MLD-Granulite	disl	5.8×10^{-21}	3.2	2.4×10^5	5	0.6	1.0×10^7
Upper Mantle MTZ	disl	2.43×10^{-16}	3.5	5.40×10^5	14	0.6	1.0×10^7
Upper Mantle MTZ	diff	1.92×10^{-11}	1.0	3.00×10^5	4.5	0.6	1.0×10^7

*Eclogite diffusion creep flow law is controlled by Equations 14-15.

Table S4. Model and main variables.

Group	Model	t_{trans}(Myr)	η_{min}(Pa·s)	Slab age (Myr)	MLD
Group1	runN00	-	-	40	No MLD
Group1	runN01	-	-	45	No MLD
Group1	runN02	-	-	50	No MLD
Group1	runN03	-	-	55	No MLD
Group1	runN04	-	-	60	No MLD
Group1	runN05	-	-	65	No MLD
Group1	runN06	-	-	70	No MLD
Group2	runR01	5	10^{18}	70	Residual
Group2	runR02	5	10^{19}	70	Residual
Group2	runR03	5	10^{20}	70	Residual
Group2	runR04	5	10^{21}	70	Residual
Group2	runR05	5	10^{22}	70	Residual
Group2	runR06	10	10^{18}	70	Residual
Group2	runR07	10	10^{19}	70	Residual
Group2	runR08	10	10^{20}	70	Residual
Group2	runR09	10	10^{21}	70	Residual
Group2	runR10	10	10^{22}	70	Residual
Group2	runR11	15	10^{18}	70	Residual
Group2	runR12	15	10^{19}	70	Residual
Group2	runR13	15	10^{20}	70	Residual
Group2	runR14	15	10^{21}	70	Residual
Group2	runR15	15	10^{22}	70	Residual
Group2	runR16	20	10^{18}	70	Residual
Group2	runR17	20	10^{19}	70	Residual
Group2	runR18	20	10^{20}	70	Residual
Group2	runR19	20	10^{21}	70	Residual
Group2	runR20	20	10^{22}	70	Residual
Group2	runR21	25	10^{18}	70	Residual
Group2	runR22	25	10^{19}	70	Residual
Group2	runR23	25	10^{20}	70	Residual
Group2	runR24	25	10^{21}	70	Residual
Group2	runR25	25	10^{22}	70	Residual
Group2	runR26	30	10^{18}	70	Residual

Group2	runR27	30	10^{19}	70	Residual
Group2	runR28	30	10^{20}	70	Residual
Group2	runR29	30	10^{21}	70	Residual
Group2	runR30	30	10^{22}	70	Residual
Group2	runR31	30	10^{22}	65	Residual
Group2	runR32	30	10^{22}	60	Residual
Group2	runR33	30	10^{22}	55	Residual
Group2	runR34	30	10^{22}	50	Residual
Group2	runR35	30	10^{22}	45	Residual
Group2	runR36	30	10^{22}	40	Residual
Group3	runRI01	5	10^{18}	70	Residual + Intrusive
Group3	runRI02	5	10^{19}	70	Residual + Intrusive
Group3	runRI03	5	10^{20}	70	Residual + Intrusive
Group3	runRI04	5	10^{21}	70	Residual + Intrusive
Group3	runRI05	5	10^{22}	70	Residual + Intrusive
Group3	runRI06	10	10^{18}	70	Residual + Intrusive
Group3	runRI07	10	10^{19}	70	Residual + Intrusive
Group3	runRI08	10	10^{20}	70	Residual + Intrusive
Group3	runRI09	10	10^{21}	70	Residual + Intrusive
Group3	runRI10	10	10^{22}	70	Residual + Intrusive
Group3	runRI11	15	10^{18}	70	Residual + Intrusive
Group3	runRI12	15	10^{19}	70	Residual + Intrusive
Group3	runRI13	15	10^{20}	70	Residual + Intrusive
Group3	runRI14	15	10^{21}	70	Residual + Intrusive
Group3	runRI15	15	10^{22}	70	Residual + Intrusive
Group3	runRI16	20	10^{18}	70	Residual + Intrusive
Group3	runRI17	20	10^{19}	70	Residual + Intrusive
Group3	runRI18	20	10^{20}	70	Residual + Intrusive
Group3	runRI19	20	10^{21}	70	Residual + Intrusive
Group3	runRI20	20	10^{22}	70	Residual + Intrusive
Group3	runRI21	25	10^{18}	70	Residual + Intrusive
Group3	runRI22	25	10^{19}	70	Residual + Intrusive
Group3	runRI23	25	10^{20}	70	Residual + Intrusive
Group3	runRI24	25	10^{21}	70	Residual + Intrusive
Group3	runRI25	25	10^{22}	70	Residual + Intrusive
Group3	runRI26	30	10^{18}	70	Residual + Intrusive
Group3	runRI27	30	10^{19}	70	Residual + Intrusive
Group3	runRI28	30	10^{20}	70	Residual + Intrusive

Group3	runRI29	30	10^{21}	70	Residual + Intrusive
Group3	runRI30	30	10^{22}	70	Residual + Intrusive
Group3	runRI31	30	10^{18}	65	Residual + Intrusive
Group3	runRI32	30	10^{18}	60	Residual + Intrusive
Group3	runRI33	30	10^{18}	55	Residual + Intrusive
Group3	runRI34	30	10^{18}	50	Residual + Intrusive
Group3	runRI35	30	10^{18}	45	Residual + Intrusive
Group3	runRI36	30	10^{18}	40	Residual + Intrusive

References:

Bondár, I. and Storchak, D., 2011. Improved location procedures at the International Seismological Centre. Geophysical Journal International, 186(3): 1220-1244.

Farla, R. et al., 2017. High-pressure, high-temperature deformation of dunite, eclogite, clinopyroxenite and garnetite using in situ X-ray diffraction. Earth and Planetary Science Letters, 473: 291-302.

Shi, F. et al., 2018. Lower-crustal earthquakes in southern Tibet are linked to eclogitization of dry metastable granulite. Nature communications, 9(1): 3483.

Storchak, D.A. et al., 2017. Rebuild of the Bulletin of the International Seismological Centre (ISC), part 1: 1964–1979. Geoscience Letters, 4(1): 32.

Storchak, D.A. et al., 2020. Rebuild of the Bulletin of the International Seismological Centre (ISC)—part 2: 1980–2010. Geoscience Letters, 7(1): 18.

Ulmer, P. and Trommsdorff, V., 1995. Serpentine Stability to Mantle Depths and Subduction-Related Magmatism. Science, 268(5212): 858-861.

van Hunen, J. and van den Berg, A.P., 2008. Plate tectonics on the early Earth: limitations imposed by strength and buoyancy of subducted lithosphere. Lithos, 103(1-2): 217-235.

Wang, J. et al., 2025. Seismic evidence for large-scale intraslab heterogeneity beneath Northeast Japan. Journal of Geophysical Research: Solid Earth, 130(4): e2024JB030046.

Wang, Y.F., Zhang, J.F., Jin, Z.M. and Green Ii, H.W., 2012. Mafic granulite rheology: Implications for a weak continental lower crust. Earth and Planetary Science Letters, 353: 99-107.

Zhang, H.L., Ravat, D. and Lowry, A.R., 2020. Crustal composition and Moho variations of the central and eastern United States: Improving resolution and geologic interpretation of EarthScope USArray seismic images using gravity. Journal of Geophysical Research: Solid Earth, 125(3): e2019JB018537.

Zhang, J. and Green, H.W., 2007. Experimental investigation of eclogite rheology and its fabrics at high temperature and pressure. Journal of metamorphic Geology, 25(2): 97-115.